



HAL
open science

Formation and evolution of glauconite in the Demerara Contourite depositional system related to NADW circulation changes during late Quaternary (French Guiana)

Cédric Tallobre, Pierre Giresse, Maria-Angela Bassetti, Lies Loncke, Germain Bayon, Roselyne Buscail, Alina Tudryn, Sébastien Zaragosi

► To cite this version:

Cédric Tallobre, Pierre Giresse, Maria-Angela Bassetti, Lies Loncke, Germain Bayon, et al.. Formation and evolution of glauconite in the Demerara Contourite depositional system related to NADW circulation changes during late Quaternary (French Guiana). *Journal of South American Earth Sciences*, 2019, 92, pp.167-183. 10.1016/j.jsames.2019.03.011 . hal-02087669

HAL Id: hal-02087669

<https://hal.science/hal-02087669>

Submitted on 22 Oct 2021

HAL is a multi-disciplinary open access archive for the deposit and dissemination of scientific research documents, whether they are published or not. The documents may come from teaching and research institutions in France or abroad, or from public or private research centers.

L'archive ouverte pluridisciplinaire **HAL**, est destinée au dépôt et à la diffusion de documents scientifiques de niveau recherche, publiés ou non, émanant des établissements d'enseignement et de recherche français ou étrangers, des laboratoires publics ou privés.



Distributed under a Creative Commons Attribution - NonCommercial 4.0 International License

1 **Formation and evolution of glauconite**
2 **in the Demerara Contourite Depositional system related to**
3 **NADW circulation changes during late Quaternary (French Guiana)**
4

5 **Cédric Talloire^{1,2,3}, Pierre Giresse^{1,3}, Maria-Angela Bassetti^{1,3}, Lies Loncke^{1,3}, Germain Bayon⁴,**
6 **Roselyne Buscail^{3,1}, Alina Tudryn⁵, Sébastien Zaragosi⁶**

7 Corresponding author: cedric.tallobre@univ-perp.fr

8
9 ¹ Univ. Perpignan Via Domitia, Centre de Formation et de Recherche sur les Environnements Méditerranéens (CEFREM), UMR 5110,
10 52 Avenue Paul Alduy, 66860 Perpignan, France.

11 ² Univ. Littoral Côte d'Opale, Laboratoire d'Océanologie et de Géosciences (LOG), UMR 8187 LOG, 52 28 Avenue du Maréchal Foch,
12 62930 Wimereux, France (present adress).

13 ³ CNRS, Centre de Formation et de Recherche sur les Environnements Méditerranéens (CEFREM), UMR 5110, 52 Avenue Paul Alduy,
14 66860 Perpignan, France

15 ⁴ IFREMER, Unité de Recherche Géosciences Marines, 29280 Plouzané, France.

16 ⁵ GEOPS, Univ. Paris-Sud, CNRS, Université Paris-Saclay, Rue du Belvédère, Bât. 504-509, 91405 Orsay, France.

17 ⁶ Université de Bordeaux, Environnements et Paléoenvironnements Océaniques et Continentaux, UMR CNRS 5805 EPOC, Allée
18 Geoffroy Saint-Hilaire - CS 50023 - 33615 Pessac cedex - France

19 **A. Abstract**

20 The Demerara Plateau is a marginal plateau which forms a bathymetric relief on the sea
21 floor. Here, contourite deposits have been studied in detail, following the recent discovery of
22 contourite sequences likely related to the bottom currents and linked both to contour current
23 and peculiar sea-floor morphology. A chronostratigraphic framework, based on $\delta^{18}\text{O}$ relative
24 variations and palaeomagnetic events in sediment cores allows correlating sediment
25 processes to current intensity changes and major climate phases (glacial or interglacial). The
26 studied sediments are enriched in glauconitic grains. In addition, the glauconite mineralogical
27 maturity can easily correlate to low sedimentation rate and slightly energetic bottom currents
28 on the seafloor. Based on these data and using the glauconitic authigenic mineral as proxy for

29 inferring the degree of winnowing at the sediment-water interface, we might put forward the
30 hypothesis that the intensity of NADW is higher during the glacial stages and lower during
31 interglacial periods.

32 Keywords: marginal plateau, contourite, glauconite, Demerara Plateau

33 **B. Introduction**

34 Contourites are sediments deposited or reworked by the action of a persistent bottom
35 current. The identification of sedimentary structures on the seafloor induced by current
36 activity introduces the concept of contourites by Heezen (1959), Heezen and Johnson (1963),
37 and Heezen and Hollister (1964). The presence of contourites is marked by a set of different
38 depositional and erosional structures at different scales. All of these structures and their
39 evolution compose a 'Contourite Depositional System' or CDS (Rebesco and Camerlenghi,
40 2008).

41 Contourites are generally characterized by a graded and often bioturbated sedimentary
42 sequence (Faugères et al., 1984; Gonthier et al., 1984; Stow et al., 2002; Stow and Faugères,
43 2008a; Rebesco et al., 2014; Shanmugam, 2016). The ideal sequence was established by
44 Faugères et al. (1984) and Gonthier et al. (1984) and completed by Stow and Faugères
45 (2008a). The alternation of positive and inverse grading sequences, composed of 5 units from
46 C1 to C5, might record velocity current variations through time. The ideal contourite
47 sequence is composed of the C1 to C5 units:

- 48 - Unit C1 is the mud unit rich in clays, in fine silt without lamination and rich in
49 bioturbation structures. This unit corresponds to a low current velocity;
- 50 - Unit C2, mottled silt and mud, is coarser than C1 with silty lenses and bioturbation;

- 51 - Unit C3 is characterized by coarsening upward sediment grain size that increases
52 Bioturbation might be strong and can destroy laminations. Erosional surfaces are
53 possible, linked to high bottom current activity;
- 54 - Unit C4: mottled silt and mud, with silty lenses and bioturbation
- 55 - Unit C5: mud unit rich in clays and in fine silt without lamination and rich in
56 bioturbation structures, and this unit correspond to a low current velocity.

57 C1 to C3 corresponds to the positive graded sequence generated by increasing current
58 intensity and C3 to C5 to the negative (inverse) graded sequence following the decrease of
59 current intensity (Faugères et al., 1984; Gonthier et al., 1984; Stow and Faugères, 2008b). The
60 sedimentation can sometimes be affected by diagenetic processes with the formation of
61 authigenic concretions such as nodules and/or encrustations of manganese, as well glauconitic
62 grains, as reported by several authors (Bahk et al., 2001; Giresse and Wiewióra, 2001; Lee et
63 al., 2004; Bahk et al., 2005; Stow and Faugères, 2008a; Faugères and Mulder, 2011).

64 According to the existing literature (Banerjee et al., 2016), the formation of glauconitic
65 grains is mainly associated to low sedimentation rate on the continental shelf whereas the
66 glauconitisation process in deep marine environments is poorly known. Some authors relate
67 the low sediment accumulation rates to winnowing effect at the sediment-water interface
68 (Chafetz and Reid, 2000; Giresse and Wiewióra, 2001; Wiewióra et al., 2001; Giresse, 2008).
69 Glaucony is a greenish grain which belongs to the glauconite mineral family, and which forms
70 inside shells (often foraminifer tests) or pellets or biotite sheets (McRae, 1972; Odin, 1988;
71 Giresse and Wiewióra, 2001; Wiewióra et al., 2001; Giresse, 2008; Banerjee et al., 2016).

72 One of the objectives of the IGUANES oceanographic cruise (2013) on the Demerara
73 Plateau (French Guiana) was to shed lights on the sedimentary processes at the origin of the
74 observed depositional sequences, possibly in relation with climate oscillations. This site has
75 been found to host a CDS, yielding sediments rich in authigenic grains of glaucony. In this

76 work, a major element analysis of the green glauconitic grains has been carried out with the
77 objective of understanding the possible role of bottom current velocity in the early diagenetic
78 processes forming glaucony and, consequently, to use this tool as a proxy for bottom current
79 intensity.

80 **C. Background of the study area**

81 The Atlantic margin of the South American continent is affected by extended contouritic
82 processes in several places, such as along the Argentina or Brazil margins (Viana et al., 1998;
83 Faugères et al., 2002; Hernández-Molina et al., 2009; Rebesco et al., 2014; Shanmugam,
84 2016). The Demerara plateau, which forms a seafloor salient prolonging the continental shelf
85 down to ~ 3400m depth (Fig.1-2), has been described as a site where bottom currents might
86 have strong control over the shape of the seafloor. The morphology of this plateau is thought
87 to be at the origin of the contourite deposits, since it might favour the acceleration of bottom
88 currents (Loncke et al., 2016; Tallobre et al., 2016).

89 **I. Oceanographic setting**

90 The Demerara Plateau is located at latitude N 7°30' between the Equator and the Tropic of
91 Cancer (Fig.1), climatically under the influence of the InterTropical Convergence Zone
92 (ITCZ), whose northern limit is at N 10° during the boreal summer (Müller-Karger et al.,
93 1989; Arz et al., 1999; López-Otálvaro et al., 2009). The main water masses controlling the
94 hydrodynamism in this area are (Reid, 1989; Peterson and Stramma, 1991; Tsuchiya et al.,
95 1994; Stramma and Schott, 1999):

- 96 - The surface water with the Tropical Surface Water (TSW) and the North Tropical
97 Gyre
- 98 - The Antarctic Intermediate Water (AAIW) formed in the Southern Ocean

99 - The deep water masses composed by the North Atlantic Deep Water (NADW) derived
100 from the North Atlantic and Arctic Seas, and the Antarctic Bottom Water (AABW)
101 formed around Antarctica (Fig.1).

102 **II. Geological setting**

103 The Demerara Plateau is a marginal plateau (Loncke et al., 2016; Mercier de Lépinay et
104 al., 2016) located at the junction between the Central and Equatorial Atlantic Oceans (Fig.1).
105 It is the conjugate margin of the Guinean Plateau. These two plateaus were initially separated
106 by a transform fault. The marginal plateau of Demerara forms an indentation, an overhang on
107 the seafloor that is 160 km wide and 350 km long (Fig.1), ranging from water depths of 200 to
108 3800 m (Fig.2).

109 This bathymetric relief hosts two main types of sedimentation along its outer edge: mass
110 transport deposit and contourites (Hurley et al., 1967; Ingram, 2006; Loncke et al., 2009;
111 Gaullier et al., 2010; Pattier et al., 2013; Loncke et al., 2016). The main mass transport
112 deposit (MTD) accumulations occurred between the Oligocene and the Pleistocene (Pattier et
113 al., 2013; Pattier et al., 2015). The associated slope failure trace is still imprinted on the
114 present-day bathymetry, forming a linear slope failure headscarp over 150 km in length that
115 parallels the distal transform marginal plateau boundary (Loncke et al., 2016).

116 The impact of the bottom current on the construction and evolution of the CDS along the
117 Demerara Plateau is highlighted by recent studies (Loncke et al., 2009; Pattier et al., 2015;
118 Loncke et al., 2016; Tallobre et al., 2016). The presence of the marginal plateau, an overhang
119 on the seafloor, enables the intensification of the NADW (NW-SE) and promotes the
120 formation of contourites on the Demerara plateau. Many erosional features, such as NW-SE
121 oriented comet marks, have been identified and attest of the impact of bottom current on the
122 seafloor structures.

123 **III. Climate general features of the study area**

124 The global climate oscillations are known through the study of various marine $\delta^{18}\text{O}$ record
125 areas in the Western Equatorial Atlantic (Arz et al., 1998; Lisiecki and Raymo, 2005; López-
126 Otálvaro et al., 2009; Lopes et al., 2014). Past climate changes in this area have driven
127 latitudinal migrations of the position of the ITCZ, generating differences in precipitation rates
128 and atmospheric humidity (Arz et al., 1999; López-Otálvaro et al., 2009; Kageyama et al.,
129 2013; Menviel et al., 2014). Particularly, during MIS 2 and MIS 4 glacial conditions, the
130 vegetation in the Guiana basin was characterized by savanna-type ecosystems (van der
131 Hammen and Absy, 1994) whereas the sea surface temperature and the atmospheric
132 temperature were $\sim 4^\circ\text{C}$ lower than present (van der Hammen and Absy, 1994; Nace et al.,
133 2014; Rama-Corredor et al., 2015). It is thought that during the ice age, the NE trade winds
134 were stronger generating a southward migration of the ITCZ and inducing drier climate
135 conditions. Consequently, the sediment discharges delivered by rivers (Maroni, Orinoco)
136 decreased in the Guiana basin due to low precipitation rates. Conversely, the Amazonian
137 basin became wetter enhancing sediment fluvial discharge from the Amazon River (Arz et al.,
138 1998; Arz et al., 1999; Mosblech et al., 2012). The hydrological activity of Maroni and the
139 Orinoco was more important during the interglacial, as consequence of the ITCZ northward
140 migration, when the Amazon basin turned into drier conditions.

141 **D. Materials and methods**

142 **I. Studied cores**

143 Three cores collected during the IGUANES cruise (2013, <http://dx.doi.org/10.17600/13010030>)
144 are studied in this work (Fig. 2):

- 145 - IG-KSF-05 (at $08^\circ 02.80\text{ N}$ and $052^\circ 23.19\text{ W}$, 3014 m water depth, 7 m in length),
146 located in the contouritic drift and most likely characterized by a continuous sediment

147 deposition. It is made of homogeneous grey-greenish mud with interbedded sandy
148 intervals (Fig.3).

149 - IG-KSF-11 (at 07°51.85 N and 052°29.25 W, 2370 m of water depth, 6 m in length),
150 located in the moat that follows the headscarp slope failure, where the current
151 influence is the strongest. This core is composed of grey-greenish mud containing
152 scattered sandy lenses (Fig.4).

153 - IG-KSF-15 (at 07°27.98 N and 052°19.76 W, 2578 m of water depth, 5 m in length),
154 located in the moat same as IG-KSF-11 but located inside a comet mark shape
155 depression. The core made of grey-greenish mud rich in green sandy grains with
156 several carbonated-rich intervals interbedded (Fig.5).

157 **II. Sediment analyses**

158 Visual descriptions on split cores were performed to identify sedimentary facies. The
159 sandy fraction ($> 63 \mu\text{m}$) was separated by wet sieving for observation under the microscope
160 in order to quantitative evaluating the sand composition.

161 Grain-size analyses were performed on bulk sediment using a Malvern Mastersizer 3000
162 with a Hydro EV wet sample disperser associated with Mastersizer application software v3.60
163 on a 1 cm step sampling resolution for core IG-KSF-11 (Fig.4). Two series of measurements
164 were generated: in bulk and carbonate-free sediment fractions. All samples (bulk sediment
165 and carbonate-free) were placed in a solution of sodium metaphosphate (NaPO_3) at 1.5 g/L to
166 deflocculate clay minerals. The distribution of size particles are used as an indicator of the
167 winnowing effect (McCave et al., 1995; McCave and Hall, 2006).

168 Semi-quantitative geochemical analyses (element count rates) were performed along core
169 IG-KSF-11 with an Avaatech X-Ray Fluorescence (XRF) core scanner (IFREMER, Brest)
170 operated at both 10 kV and 30 kV and with a 1 cm sampling interval. In this study, Ca has
171 been used to provide information about the biogenic components.

172 **III. Glauconite study; quantification and analyses**

173 The quantification of glauconitic grains was carried out on the sandy fraction every 10 cm
174 in cores IG-KSF-11 (Fig. 4) and IG-KSF-15 (Fig. 5). The glauconitic grains were isolated
175 under the microscope. Those were weighed and the weight was normalized with respect to 1)
176 the sandy fraction and 2) the bulk sediment and then expressed as a percentage (%). The
177 glauconitic grains were classified into three colour categories: yellowish-green, green, and
178 dark green (visual estimation), the last one being sub-divided into dark and very dark green
179 Representative samples were selected on core IG-KSF-11 for SEM observation, using a SEM
180 HITACHI S-4500. These samples (104 grains) were collected at different intervals on IG-
181 KSF-11: 0 cm, 50 cm, 270 cm, 300 cm, 450 cm, 460 cm and 590 cm. Quantitative elementary
182 analyses were performed using a SEM-EDS system. Two measurements were carried out at
183 the surface of each grain. These samples were collected at different intervals on IG-KSF-11:
184 50 cm, 270 cm, 300 cm, 450 cm, 460 cm and 590 cm. To complete this study, 9 additional
185 samples on the 0 and 100 cm interval on IG-KSF-11 and one on the top of IG-KSF-15) were
186 analysed for X-ray diffraction (Philips) on the < 2 µm fraction for clay minerals.

187 Four thin sections from indurated sediment were obtained in the IG-KSF-11, following
188 the method described by Zaragosi et al. (2006). The selected intervals are: 20-40 cm; 337-
189 367 cm; 449-479 cm; 580-600 cm (glauconite rich horizons). Thin sections have been
190 observed under transmitted polarizing microscope for micro-facies description.

191 **IV. Chronostratigraphy**

192 Radiocarbon dates in different cores (IG-KSF-05 and IG-KSF-11) were obtained by
193 Accelerator Mass Spectrometry (AMS) at the Poznań Radiocarbon Laboratory, using
194 monospecific assemblages of well-preserved planktic foraminifer *Globigerinoides sp.*
195 Measured ages were converted to calendar years using Calib 7.0.4 with the Marine 09
196 calibration curve (Reimer et al., 2013).

197 Oxygen stable isotope ratios were measured on samples from cores IG-KSF-11 and IG-
198 KSF-05 using a 5 cm sampling step. These measurements were carried out on benthic
199 (*Uvigerina mediterranea*) and planktonic (*Globigerinoides ruber* and *Globigerinoides sp.*)
200 foraminifera at the Leibniz Laboratory for Radiometric Dating and Stable Isotope Research
201 (Kiel, Germany).

202 Magnetic parameters allow an identification of the magnetic field at the time of sediment.
203 NRM and isothermal remanent magnetization (IRM) measurements were made on cores IG-
204 KSF-05 and IG-KSF-11, on U-channels (at 2 cm intervals) with a horizontal 2G Entreprises
205 pass-through cryogenic magnetometer. NRM was demagnetized with an AF up to 80 mT
206 using the in-line mounted alternating field (AF) demagnetizer. IRM was introduced in 1 T and
207 -0.3 T fields, and the S-ratio ($IRM_{-0.3T}/IRM_{1T}$) was calculated.

208 E. Results

209 I. Chronostratigraphy

210 A multiproxy study was necessary to establish a chronostratigraphic framework. The steps
211 followed for establishing a depth-age profile are described below, together with comments
212 about the difficulties encountered.

213 1. Radiocarbon data

214 IG-KSF11:

215 In core IG-KSF-11 from 0 to 190 cm depth the ^{14}C ages range from 14 kyr BP to 50 kyr
216 BP (Table 1), without any anomaly. The sediment accumulation rates calculated for this
217 interval are:

- 218 - 0 - 60 cm: 2.7 cm/kyr
- 219 - 60 - 130 cm: 23 cm/kyr
- 220 - 130 - 190 cm: 5.5 cm/kyr.

221 The first stratigraphically incoherent age occurs at 313 cm with 43 kyr cal BP, followed by
222 the 530 cm level, where two different ages are obtained (49 kyr BP and 26 kyr BP). The
223 second measurement was performed on bulk sediment. Unfortunately, this material does
224 not contain enough organic matter for accurate dating. Other stratigraphically incoherent
225 ages are found at the bottom of the core at 582 cm (39 kyr BP) and 600 cm (28 and 35 kyr
226 BP). The base of the core (600 cm) was measured twice and the resulting ages are largely
227 different with a gap of 7 kyr.

228 IG-KSF-05:

229 The upper part of core IG-KSF-05 (0 cm) is dated at 5.6 kyr BP. The ages obtained deeper
230 range from 44 kyr to 5.6 kyr (table 1) and give the following sediment accumulation rates:

- 231 - 0 – 29 cm: 2.4 cm/kyr
- 232 - 29 – 50 cm: 1.2 cm/kyr
- 233 - 50 – 169 cm: 33.9 cm/kyr

234 Some stratigraphic incoherencies are also present in this deeper part of the core (Table 1):
235 37.9 kyr BP at 169 cm, 30.6 kyr BP at 250 cm, 44 kyr BP at 340 cm and 41 kyr BP at 490 cm.

236 Thus, the stratigraphic incoherence and the strong difference in the sedimentation rates
237 highlight the anomaly of dating, especially in the lower part of the two cores.

238 **2. Stable isotopes and chronostratigraphy**

239 Tie points have been identified comparing the relative oxygen isotope variations in the two
240 cores studied in this work (Fig.6, table 2), in order to correlate them with Marine Isotope
241 Stages (MIS).

242 The regional curves used here as references are (Fig.6):

- 243 1) oxygen isotope ratios from core MD03-2616 recovered in the Guiana Basin at a
244 water depth of 1233 m and published in López-Otálvaro et al. (2009);

245 2) the Atlantic Ocean compilation from Lisiecki and Raymo (2005), (2009);

246 3) oxygen isotope ratios from core GeoB 3104 from a water depth of 767 m in the

247 North Brazilian margin (Arz et al., 1998).

248 - **MIS 1 (0-11.7 kyr):** The core-tops of IG-KSF-11 and IG-KSF-05 (0 cm) do not

249 correspond to modern ages, possibly because the upper part of the sediment column

250 was lost during coring. A rapid increase of $\delta^{18}\text{O}$ values is observed at 10 cm depth in

251 core IG-KSF-11 and at 18 cm depth in core IG-KSF-05, which can correlate with the

252 beginning of MIS 1.

253 - **MIS 2 (11.7-24.1 kyr):** Between 10 and 43 cm with a sedimentary accumulation rate

254 of $2.7 \text{ cm}/10^3 \text{ yr}$ in core IG-KSF-11 and 18 and 139 cm with a rate of $9.2 \text{ cm}/10^3 \text{ yr}$ in

255 core IG-KSF-05, relatively high positive $\delta^{18}\text{O}$ values are thought to correspond to the

256 MIS 2 cold stage. The low resolution of the isotope measurements does not allow us to

257 precisely identify the glacial maximum, but the correlation with Arz et al. (1998)

258 isotope curve, suggests that the LGM could be positioned at 20 cm depth in IG-KSF-

259 11 and at 35 cm depth in IG-KSF-05 (Fig.6);

260 - **MIS 3 (24.1-58.9 kyr):** The interval comprised between 43 and 80 cm in IG-KSF-11

261 ($1 \text{ cm}/10^3 \text{ yr}$) and between 139 and 451 cm in IG-KSF-05 ($8.7 \text{ cm}/10^3 \text{ yr}$) is tentatively

262 assigned to MIS 3. However, its features cannot be directly compared to the global

263 curves (Fig.6), mainly because of the occurrence of relatively negative values obtained

264 in planktonic and benthic foraminifera in both cores (Fig.6). These oscillations are not

265 evident at the global scale but are nonetheless observed regionally, as illustrated in

266 López-Otálvaro et al. (2009);

267 - **MIS 4 (58.9-74 kyr):** This (moderate) glacial stage is located in the 80-150 cm

268 interval in core IG-KSF-11 ($4.6 \text{ cm}/10^3 \text{ yr}$) and in the 451-590 cm interval in core IG-

269 KSF-05 ($9.2 \text{ cm}/10^3 \text{ yr}$), based on the relative $\delta^{18}\text{O}$ variations compared to MIS 3

270 (Fig.6). The pattern of isotope ratio values is considered coherent and comparable with
271 the global temperature trends;

272 - **MIS 5 (74-130 kyr)**: The interval between 150 and 267 cm in IG-KSF-11 and 590 and
273 694 cm in IG-KSF-05 is assigned to MIS 5. The MIS 5 is subdivided into five sub-
274 stages (MIS 5.1 to MIS 5.5) that are recorded in many areas of the ocean (Shackleton
275 et al., 2003) where the MIS 5.5 consists in the most prominent temperature rise
276 (Fig.6). In core IG-KSF-11, two intervals show considerably negative $\delta^{18}\text{O}$ values (at
277 160-200 cm depth and 235-365 cm depth, Fig.6) that could possibly match the MIS
278 5.1 and 5.3. Thus, the basal prominent peak would be missing. The reason why it is
279 lacking is not clear, but a non-depositional or even an erosional episode is possible.

280 - **MIS 6 (130-189.6 kyr) and MIS 7 (189.6-244 kyr)?**: Below MIS 5, the correlation
281 becomes really uncertain. A possible assignment of the interval comprised between
282 267 and 371 cm in core IG-KSF-11 to MIS 6 is proposed, since the relatively positive
283 $\delta^{18}\text{O}$ values might be consistent with a glacial stage (Fig.6), but there is no other proxy
284 that could confirm this hypothesis. Even more difficult is the interpretation of the
285 interval below 380 cm depth in core IG-KSF-11 (Fig.6) since it is possibly affected by
286 heavy reworking. In an optimistic view, it could be possible to consider that the
287 interval comprised between 371 and 422 cm depth might belong to MIS 7, but with no
288 certitude. On the other hand, below 430 cm depth, the sediment is fully reworked. The
289 question, which remains open in this work, is when this reworking took place, either
290 during the glacial stage (MIS 8), the interglacial (MIS 7), or later.

291 **3. Palaeomagnetism**

292 As shown by Bleil and Von Dobeneck (1999), the natural remanent magnetization (NRM)
293 can record the direction (declination and inclination), the relative palaeointensity and the
294 geomagnetic event during the Late Quaternary. In marine environments, the ferromagnetic

295 detrital minerals such as magnetite and hematite become aligned by the geomagnetic field as
296 they fall through the water and become part of the sediment on the bottom of the sea; it is the
297 detrital remanent magnetization (DRM) that often contributes predominately to the NRM in
298 such marine sediments.

299 In the cores IG-KSF-11 and IG-KSF-05, the NRM decrease during the demagnetisation
300 and the S-ratio values varying between 0.9 and 0.8 indicate that the magnetic fraction of the
301 sediment is dominated by minerals of low coercivity such as magnetite, with minor amounts
302 of higher coercivity minerals - hematite or goethite (Tudryn et al., 2010). In the bottom (600 -
303 450 cm depth) of the core IG-KSF-11, slightly lower S-ratio values (0.7 - 0.8) indicate
304 increased contents of the hematite and/or goethite. NRM shows stability in direction and low
305 inclination values, except in the bottom of the core IG-KSF-11 (Fig. 4) and the top of IG-
306 KSF-05 (Fig. 3). On the top of the core IG-KSF-05, an important variation in declination and
307 inclination is recorded around the transition between MIS 1 (0-18 cm) and MIS 2 (25-139 cm)
308 as identified through $\delta^{18}\text{O}$ record (above); it likely corresponds to the Gothenburg
309 Geomagnetic Polarity Excursion at 12.5 kyr (Mörner, 1977; Barbetti et al., 1980; Mörner,
310 1986), described between 12.5 and 13.5 kyr in European and Cameroon lakes (Smith and
311 Creer, 1986; Thouveny and Williamson, 1988; Maley et al., 1990). The Laschamp event,
312 around 40 kyr (Bonhommet and Babkine, 1967; Guillou et al., 2004; Plenier et al., 2007), and
313 the Blake event, around 119 kyr (Lund et al.; Smith and Foster, 1969; Gibbard and Cohen,
314 2008), seem to be absent or not identifiable in the studied successions. Nonetheless, the
315 stability of magnetic parameters suggests that the sediment was not affected by post-
316 depositional reworking, except for the basis of IG-KSF-11 and probably the top of IG-KSF-
317 05.

318 **II. Grain size analysis**

319 In the core IG-KSF-11 (Fig.4), the average clay content is 20% of the total sediment,
320 while the fine silt-size fractions account for between 40 and 60% and hence constitute the
321 dominant fraction. Coarse silt and sand correlate to Ca relative content suggesting that this
322 relatively coarse fraction is made of biogenic carbonates, relatively abundant during estimated
323 ice periods (MIS 2-4-6; Fig.4).

324 The free carbonate \overline{SS} varies between 15 μm and 30 μm (Fig.4). With respect to the bulk
325 sediment grain-size plot, the \overline{SS} is high between 420-600 cm and the bottom of the core. The
326 values increase during the ice period MIS 6 (267-371 cm) and decrease to relatively low
327 values during MIS 5 (150-267 cm). Some higher values correspond to the 200-230 cm
328 interval and are associated with an increase in isotopic values. The \overline{SS} becomes high from
329 MIS 4 and through the 'weak' MIS 3 interglacial (Fig.4).

330 **III. Facies**

331 **1. Analysis**

332 Seven sedimentary facies have been identified after visual description of all cores
333 (Tallobre, 2017), combined with observations of thin sections on core IG-KSF-11 (Table 3).
334 They are described as follows:

- 335 - **F1 Carbonate facies** with indurated foraminifera-rich carbonate (Table 3, Fig.5). This
336 F1 corresponds to remobilized sediment blocks, which are dated to the Oligocene-
337 Miocene period (Tallobre, 2017). This slope instability event has also been described
338 further Northwest by Ingram et al. (2011).
- 339 - **F2 Glauconitic sand** composed by glauconitic sand (20-30%) and biogenic debris
340 (mainly foraminifera). Glauconitic grains are dominant and constitute up to 94% of the
341 sandy fraction (Table 3, Fig.7A- 7B-8C). Laminae, sand lenses and bioturbation can be

342 observed. Glauconite can (1) infill foraminifer tests whose the moulds can be
343 preserved (Fig.7B, 8C) or (2) form infra-millimetric clasts (Fig.7C-7F). The latter
344 show a high degree of fracturing, irregular shape and they can derive from erosion and
345 transport of slightly lithified glauconitic beds hardground.

346 - **F3 Sandy facies.** It is characterized by bioturbated foraminifera-rich sand mixed with
347 glauconitic grains (between 0.1% and 1% of highly fractured glauconite grains in the
348 sandy fraction, and around 20 % of sand and coarse silt) and joined grains as
349 illustrated on the thin section (Table 3, Fig.7C-8E). Laminae or sand lenses can be
350 found (Fig.7C).

351 - **F4 Foraminifera- and glauconitic-bearing muddy facies** with slightly laminated
352 foraminifera rich mud (Table 3), few glauconitic grains (with a proportion lower of
353 0.1%) in the sand fraction (Fig.7D-8D). It can be differentiated from F3 because of the
354 low content of sandy grains and because glauconitic grains are less abundant in the
355 mud and concentrated in bioturbation (Fig. 8A-8B).

356 - **F5 Foraminifera sand** composed by foraminiferal sandy facies (20% of sand and
357 coarse silt) with joined grains and poor in glauconitic grains (Table 3, Fig.7E). The
358 fracturing of grains is moderate to low.

359 - **F6 Foraminifera-bearing muddy facies** similar to F5, (rich in foraminifera and rare
360 glauconitic grains). The distinctive difference lies in the proportion of sandy grains
361 (Table 3) that are diluted in the mud and not joined (Fig.7F).

362 - **F7 Muddy facies** composed by massive mud (Table 3, Fig.7G) with low foraminifera
363 and rare glauconitic grains.

364 **2. Comments**

365 Some of the described facies record contrasted hydrodynamic conditions and may
366 correspond to a local expression of the ideal contouritic sequence. In particular:

- 367 - F2 Glauconitic sand and F3 Sandy facies, based on grain size and grain fracturing,
368 associated to degraded organic matter (Tallobre et al., 2016), are characteristic of high
369 winnowing conditions and may correspond to an equivalent of the C3 contourite
370 sequence.
- 371 - F4 Foraminifera- and glauconitic-bearing muddy facies, poorer in sandy grains may
372 relate to the upper part of C2 with an increasing winnowing effect, whereas the lower
373 part of C4 should correspond to decreasing winnowing effect.
- 374 - F5 Foraminifera sand and F6 Foraminifera-bearing muddy facies, with quite abundant
375 foraminifera tests (the sandy fraction) may correlate to the lower part of C2 and the
376 upper part of C4 and a moderate winnowing effect.
- 377 - Finally, F7 Muddy facies, the finest in terms of grain size, probably corresponds to an
378 equivalent of units C1 and C5. The good organic matter preservation in this facies is
379 consistent with very low winnowing effect (Tallobre et al., 2016).

380 **IV. Glauconite study**

381 **1. Glauconitic grain facies and contents**

382 Sediments collected in the moat are rich in glaucony (Fig.4-5). On the contrary, sediment
383 from the contouritic drift, as IG-KSF-05 (Fig.3), contain less glauconitic grains and
384 sometimes abundant pyrite can be found (usually anti-correlating the glauconite content).

385 a. *Core IG-KSF-11*

386 Vertical distribution of glauconitic grains for IG-KSF-11 (Fig.4) has been compared to
387 $\delta^{18}\text{O}$ ratios for correlation with the glacial/interglacial intervals previously defined:

- 388 - Between 500-601 cm (chronologically undefined interval), the sediments have a
389 moderate content in glauconitic grains (0.08% on average for the bulk sediment), with

390 17% of yellowish-greenish, 42% of green and 41% of dark green grains (with the
391 green shade illustrated in Fig.4);

392 - Between 400 and 500 cm (reworked and chronologically undefined interval two high
393 glauconitic grain content peaks stick out (430-440 cm and 480-490 cm): 11% and 13%
394 in the bulk sediment and 94% and 91% in the sandy fraction (facies F2). The dark
395 green grains represent 95-96% of glauconitic grains;

396 - In sediment corresponding to glacial stages (10-43 cm in MIS 2, 80-150 cm in MIS 4
397 and 267-371 cm in MIS 6), the green grain content is moderate (facies F3-F4) to high
398 (facies F2). This is particularly true in the MIS 6 sediments where the green grain
399 content reaches 1.2% in bulk sediment and 25% of the sandy fraction. Yellowish-
400 greenish grains are less abundant (up to 15% in the 267-371 cm interval), whereas
401 green grains and dark green grains reach high concentrations (50% and 40%,
402 respectively). As a general trend, the abundance of glauconitic grains decreases
403 upward from the beginning of the glacial stage (Fig.4).

404 - The interglacial periods (43-80 cm in MIS 3, 150-267 cm in MIS 5, and part of MIS 7
405 at 371-400 cm) are characterized by low glauconitic contents (sometimes completely
406 absent, facies F6-F7). When glauconitic grains are present, they are generally
407 yellowish to greenish. The Holocene (0-10 cm) yields moderate glauconitic content of
408 0.04 to 0.09% of the bulk sediment (50% of green and dark green grains, with up to
409 80% of dark green at the top of the core).

410 b. *Core IG-KSF-15*

411 In core IG-KSF-15 (Fig.5), the interval between 170-470 cm is composed of an alternation
412 of silty-clay and silty-sandy beds, all rich in glauconitic grains with 47% of dark green and
413 26% of green grains corresponding to facies F2. The interval corresponding to 120-170 cm is
414 made of carbonated reworked sediment (facies F1). Although some glauconitic grains are

415 present between 170-160 cm, the glauconitic concentration remains poor. The top of the core
416 (0-120 cm) is characterized by fine sediments with low content in glauconitic grains (facies
417 F4) and 50% of yellowish-greenish grains.

418 **2. SEM observations and microprobe analysis on glauconitic grains**

419 Under the SEM observation, it has been possible to correlate the increasing colour
420 darkness to the presence of cracks at the surface of the grain (Fig.9). These cracks become
421 more abundant and deeper as the grains get darker. Micro-sheets are also observed, more
422 numerous and more distinct as the green colour becomes darker. They can eventually form a
423 'rose' structure (Fig.9). These neo-formed sheets gradually fill the intra-grain porosity.

424 Elementary analyses were performed and compared for the four colour categories of
425 glauconitic grains visually defined. The averages of results for major element compositions
426 are presented in table 4. The reference mud samples collected correspond to beds with less
427 than 0.1% of green grains. In the mud, the high value in Al_2O_3 suggests the occurrence of
428 kaolinite, but this oxide can also be found too in illite and smectite. The Mg is generally found
429 in smectite, and to a lesser extent in illite.

430 On the basis of the obtained results, hereafter the points that can be highlighted:

- 431 - Marine mud, on the top of core IG-KSF-11, analysed by X-Ray diffraction, is
432 composed by 25% of smectite, 35% of illite and 40% of kaolinite. The content in
433 Al_2O_3 is 18.1%, 9% for Fe_2O_3 , and 2.5% for K_2O (Fig.10).
- 434 - In greenish/yellowish grains, the content in Al_2O_3 decreases at 8.8%, whereas it
435 increases for Fe_2O_3 to 27% and for K_2O to 2.9% (Fig.10).
- 436 - In green grains, the content in Al_2O_3 decreases again at 7.4%, the increasing keep up
437 for Fe_2O_3 to 30.3% (and punctually until 33.4% on Fig.9) and for K_2O to 3.2%
438 (Fig.10).

439 - The trend continues for dark green grains: decrease for Al₂O₃ at 5.6%, and increase for
440 Fe₂O₃ to 34% and for K₂O to 4.3% (Fig.10).

441 - For very dark green grains, the content in Al₂O₃ (5.8%) and in Fe₂O₃ (34.2%) vary
442 only slightly whereas the content in K₂O continue to progress in average to 5.8% (Fig
443 10) and punctually until 6.5% in K₂O (Fig.9).

444 The greening process is characterized by a rapid and strong increase of iron (Fig.10). The
445 potassium also increases, more slowly and keeps up longer than iron.

446 **F. Discussion**

447 The main weak point in this study is the uncertain chronostratigraphic framework. It has
448 been established by putting together information inferred from different proxy data but it is
449 far from being perfect. Unfortunately, all possible dating methods (applicable to this site) do
450 not allow 1) building a more precise age model; 2) to identify with precision the presence and
451 duration of sediment hiatuses. The uncertainties remain significant, especially before MIS 5.
452 Because of the impossibility of obtaining a better precision, we have limited the
453 chronostratigraphy to the identification of glacial and interglacial stages proposing a
454 correlation with isotope stages, as described in the paragraph 2, in order to describe the
455 mechanisms at the origin of glauconite formation in the contourite sequences and their
456 possible relation with climate. Despite the significant difficulty to establish a solid
457 chronostratigraphic framework before MIS 5, the studied cores represent quite exceptional
458 sediment archives for correlating the phenomenon of glauconite formation and to establish to
459 what extends this feature can be used as a reliable proxy for paleoceanographic
460 reconstructions.

461

I. Glauconitisation process

462

1. Formation and maturation of green grains

463

464

465

466

467

468

469

470

471

472

473

During glauconitisation, the enrichment in K (from 2.9% to 5.8% K₂O, Fig.9-10) and Fe (from 27% to 34.2% Fe₂O₃) occurs at different rates with glauconite maturation (table 4). The greening of grains expresses enrichment in Fe-smectite and interstratified Fe-smectite/glauconite. The diachronic evolution, between Fe and K, illustrates the fact that iron is incorporated and oxidized rapidly, whereas K assimilation is a slightly slower process (Fig.10 and table 4). This greening is characterized first, by Fe-smectite neoformation, and then, by neoformation of interlayered minerals. Incorporation of Mg, Fe and K in the mineral structure (Fig.9) is the way to transform smectite into Fe-smectite and then into interstratified Fe-smectite/glauconite. It expresses the chemical evidence of the maturation process of glauconitic grains (Odin, 1988; Giresse and Wiewióra, 2001; Wiewióra et al., 2001; Giresse, 2008; Baldermann et al., 2013; Baldermann et al., 2015; Banerjee et al., 2016).

474

475

476

477

478

479

480

481

482

483

484

485

Greening is controlled by the chemical evolution and oxidation state of Fe. Ferrous Fe is at the origin of the grains green colour and its oxidation in Fe-ferric is responsible for the darkening. The elementary composition is the indicator of mineralogical evolution phases (Fe-smectite, interstratified Fe-smectite/Glauconite, and glauconite). The chemical evolution, and thus the greening, are related to the development of numerous micro-sheets (illustrated on the SEM pictures on the Figure 9) infilling the intra-grain porosity. These characteristics indicate the maturity of glauconitic grains. The multiplication of Fe-smectite and interlayered micro-sheets (see SEM pictures on Fig.9) generates density variations (between original mud and the different mineralogical states (Giresse, 2008)). The greening process is associated with the neoformation of interstratified Fe-smectite/illite by the incorporation of K. The neoformed Fe-smectite, which are hydrated, are less dense. This growing neoformation of hydrated minerals causes the decrease of density and increase of volume. Hence, the

486 neoformation generates a pressure inside green grains which induces cracking at the grain
487 surface, well developed and clearly shown on the SEM pictures (Fig.9). These cracks are thus
488 an indicator of the mineralogical maturity of glauconitic grains (Giresse, 2008).

489 **2. Glauconitisation at the sea/surface interface**

490 The analyses performed on green grains indicate a geochemical trend and that the
491 greening is accompanied by elementary and mineralogical changes (Fig.9-10).

492 However, the limiting factor for glauconitisation is the availability of Fe (supplied by the
493 alteration of minerals of continental origin) and K (directly provided by sea water). In the
494 anoxic mud of deep-sea sediments, iron is mainly present as Fe²⁺. The rapid oxidation of
495 organic matter causes a redox front between the grain and the surrounding mud, making the
496 micro-environment around the foraminifera more oxidising than the mud matrix (Odin, 1988;
497 Giresse and Wiewióra, 2001; Wiewióra et al., 2001; Giresse, 2008). Thus, Fe²⁺ migrates
498 rapidly inside foraminifera tests, where it is partly oxidized into Fe³⁺ and possibly
499 incorporated into octahedral structures; smectites become Fe-smectites (Fig.10.1 and 10.2).
500 This process occurs relatively rapidly at the water/sediment interface. In contrast to Fe, K
501 migrates slowly and gradually from seawater into the micro-environment inside buried
502 foraminifera tests below the seafloor to form glauconite assemblages (Fig.10). The interlayer
503 incorporation of K, and consequently glauconitisation, requires a long exposure period at the
504 sea water/sediment interface. If these two conditions are filled, the transformation of detrital
505 clay minerals into Fe-smectite, interlayered Fe-smectite/glauconite and glauconite is possible
506 (Fig.10). The formation of mature glauconitic grains, composed of Fe-smectites and
507 interlayered Fe-smectite/glauconite (with 5% to 6.5% K₂O in our samples Fig.9), occurs
508 rapidly during the early diagenetic process (about 10 to 100 kyr). The complete
509 glauconitisation process (with more than 8% of K₂O expected (Giresse, 2008)) needs a longer
510 period of time, ranging from 2 to 10 Myr (Odin and Fullagar, 1988; Odin, 1988; Gaudin et al.,

511 2005; Baldermann et al., 2013), and as such often happens during late marine diagenetic
512 processes.

513 **3. Glauconitisation and winnowing effect**

514 During early diagenesis, glauconitisation occurs at the water/sediment interface with low
515 sedimentation rates to promote the incorporation of Fe and subsequently K (McRae, 1972;
516 Odin, 1988; Giresse and Wiewióra, 2001; Wiewióra et al., 2001; Giresse, 2008). At times,
517 low sedimentation rates can be induced by the winnowing effect linked to bottom current
518 activity (Chafetz and Reid, 2000; Giresse and Wiewióra, 2001; Wiewióra et al., 2001;
519 Giresse, 2008).

520 In Demerara contouritic sediments, the glauconitic facies (F2) are characterized by high
521 sandy and silt content, high value of \overline{SS} , high fracturing of grains, and an enhanced
522 degradation of organic matter (Tallobre et al., 2016). These elements suggest that the
523 glauconitisation might be related to high winnowing effect. Moreover, the here described
524 glauconitic facies corresponds to sediments collected in the moat (Fig.4-5) stronger bottom
525 water winnowing) whereas this facies is absent in sediments collected in the drift (Fig.3,
526 weaker bottom water winnowing, finer sediments and rare glauconite fracturing features).

527 As a consequence, we put forward the hypothesis that during the period characterized by
528 the highest current intensity, the winnowing effect inhibits sediment deposition and instead
529 causes erosion at the seafloor and high fracturing of foraminifers' tests. The mud directly in
530 contact with seawater, is more oxidising than in the underlying mud, which can promote the
531 occurrence of a redox front and, likely, glauconitisation (Fig.10).

532 Glauconitisation at the seafloor is concomitant to the formation of indurated beds.
533 Occasionally, during the erosional phases, some coarse clasts can be reworked from the
534 seafloor, deposited and mixed within the glauconitic sandy facies as intraclasts (facies F2,
535 Fig. 8C-8F).

536 **II. Glauconite and contourite sequence**

537 The link between glauconitic grain maturity, winnowing effect and current intensity
538 allows us to propose an alternative ‘ideal’ contouritic sequence that integrates the glauconite
539 content and its degree of maturity (Fig.11). Thus, units C1 and C5 might correspond to low
540 current velocity muddy facies, with a low glauconitic grain content and maturity (Fig.3 and
541 4). The C2 and C4 mottled muddy facies should record current velocity decrease and
542 subsequent increase, corresponding to negatively and positively graded sediments. Those
543 facies contain abundant glauconitic grains including a mixture of different green grains with
544 dominance of dark green and light green grains. The dark green grain concentration increases
545 with coarsening in C2, and it decreases in the fining upward of C4, and inversely for
546 yellowish-greenish grains (Fig.3, 4 and 5). Finally, the C3 sandy facies corresponding to the
547 maximum current velocity is characterized by a high content of dark green grains as
548 illustrated along the cores (Fig.3, 4 and 5). At the maximum of bottom current intensity,
549 during low sedimentation, hardground surfaces might form with possible erosion and
550 formation of glauconitic intraclasts.

551 **III. Winnowing effect and current velocity Quaternary evolution**

552 While the evolution of the NADW intensity is still subject to discussion, the results
553 obtained in this study for the Demerara Plateau (IG-KSF-11 and IG-KSF-05) provide further
554 evidence on the factors that may have affected the strength of deep-ocean circulation and its
555 effect on sedimentation in the equatorial western Atlantic. It is necessary to bear in mind that
556 the chronostratigraphic framework obtained on the studied cores is not sufficiently robust for
557 being considered conclusive. However, based on the $\delta^{18}\text{O}$ relative variations and
558 palaeomagnetic records, we propose the distinction between glacial vs interglacial intervals in
559 these cores, in order to discuss the evolution of bottom currents according to climate
560 conditions.

561 To resume the features observed in the sediments, the glacial stages are characterised by:

- 562 - relative high glauconitic grain content;
- 563 - high maturity of glauconitic grains;
- 564 - sandy facies, rich in sand and coarse silt;
- 565 - high degree of fracturing of the shell debris and glauconitic grains;
- 566 - largely winnowed organic matter.

567 Within the intervals corresponding to the full interglacials, it is possible to observe:

- 568 - moderate to very low glauconitic content,
- 569 - low maturity of glauconitic grains,
- 570 - muddy facies, rich in clays and fine silt
- 571 - low degree of fracturing of shells,
- 572 - better preservation of organic matter.

573 Taken together, the observed differences between glacial and interglacial sediment
574 characteristics suggest that global climate exerts a strong control on contourite deposition and
575 associated diagenetic processes. Evidence of a high winnowing effect, which coincided with
576 low sedimentation rates caused by a high current velocity, would be consistent with the
577 hypothesis of a vigorous bottom current activity during the glacial periods (Curry and Oppo,
578 2005; Böhm et al., 2015; Lippold et al., 2016).

579 Particularly, the degree of glauconite maturity in the cores studied in this work, suggests
580 the presence of an active overturning circulation during the glacial phases in this segment of
581 Atlantic Ocean. Lippold et al. (2016) evidenced the persistence of a vigorous oceanic
582 circulation during the LGM in the relatively shallow (>2000 m depth) Southern Atlantic, but
583 the case of Demerara Plateau is even more peculiar, because of its particular morphology. As
584 stated before, the large indentation is thought to be at the origin of the intensification of the
585 NADW, favouring the formation of contourites (Tallobre et al., 2016). Here, we put forward

586 the hypothesis that during glacial stages, the action of overturning circulation could have been
587 amplified by the Demerara Plateau morphology, inducing a strong and prolonged winnowing
588 on sediments as testified by the glauconite neoformation.

589 **G. Conclusion**

590 This study describes the characteristics of deposits belonging to contourite sequences on
591 the Demerara Plateau, through the detailed analyses of sediment cores retrieved during the
592 IGUANES cruise. A very distinctive sediment feature is the presence of an authigenic
593 mineral, the glauconite, that here is thought to be formed under the effect of bottom water
594 hydrodynamic conditions, since the formation of glaucony might be relatively rapid at the
595 water/sediment interface during the first stage of diagenesis.

596 In particular, the winnowing effect is very likely at the origin of the formation of
597 glauconite (composed of Fe-smectite and interlayered Fe-smectite/glauconite) that is observed
598 to develop mainly inside foraminifera tests at the sediment-water interface.

599 The detailed study of glauconite grains allowed to identify the different phases of the
600 glauconitisation process, and characterized by (1) increasing relative abundance of glauconitic
601 grains and (2) increasing degree of mineralogical maturity.

602 The degree of maturity has been defined by (a) grain colour (yellowish green for immature
603 glauconite to dark green for very mature glauconite), (b) the presence of cracks at the grain
604 surface, together with the enrichment in neoformed microstructures and decreasing porosity
605 inside grains and (c) by mineralogical and chemical composition change. The formation of
606 glaucony is relatively rapid at the water/sediment interface during the first stage of diagenesis.

607 Hence, the features of glauconitic grains are here used as an indicator of the winnowing
608 effect. This *proxy* is thought to have a good potential since it allows a semi-quantitative

609 estimation of the current intensity and, combined with other sedimentological and
610 geochemical parameters, could have an interest in studies of contouritic deposits.

611 In this study, the characteristics of glauconitic sediments and their correlation with the
612 major climate shifts, suggest that the NADW flow was strengthened during glacial periods,
613 likely because the local morphology (indentation of the Demarara Plateau) may have
614 generated a strong and prolonged bottom water winnowing.

615 H. Acknowledgments

616 The authors would like to thank the crew of the N/O L'Atalante. We also thank Shell and
617 Ifremer for supporting Cédric Talloire's PhD Project, Ifremer Brest laboratories for technical
618 support on sediment core handling and analyses (Angélique Roubi, Mikael Rovere, Joël
619 Etoubleau); Bernard Martin at the University of Bordeaux the thin sections; the CEFREM
620 (University of Perpignan), Christophe Menniti, Bruno Charrière, Jennifer Sola, Stéphane
621 Kunesch, Christine Sotin for access to laboratory facilities and assistance. Many thanks to the
622 graduate students who worked on this topic: Camille Ferrer, Lea Bonnin, Simon Faye,
623 Emmanuel Chassagnac. Finally, authors thank reviewers and editors for their contributions to
624 improve this paper.

625 I. References

- 626 Arz, H.W., Pätzold, J., Wefer, G., 1998. Correlated Millennial-Scale Changes in Surface
627 Hydrography and Terrigenous Sediment Yield Inferred from Last-Glacial Marine Deposits off
628 Northeastern Brazil. *Quaternary Research* 50, 157-166.
- 629 Arz, H.W., Pätzold, J., Wefer, G., 1999. Climatic changes during the last deglaciation
630 recorded in sediment cores from the northeastern Brazilian Continental Margin. *Geo-Marine*
631 *Letters* 19, 209-218.
- 632 Bahk, J.J., Chough, S.K., Jeong, K.S., Han, S.J., 2001. Sedimentary records of
633 paleoenvironmental changes during the last deglaciation in the Ulleung Interplain Gap, East
634 Sea (Sea of Japan). *Global and Planetary Change* 28, 241-253.
- 635 Bahk, J.J., Lee, S.H., Yoo, H.S., Back, G.G., Chough, S.K., 2005. Late Quaternary
636 sedimentary processes and variations in bottom-current activity in the Ulleung Interplain Gap,
637 East Sea (Korea). *Marine Geology* 217, 119-142.

638 Baldermann, A., Deditius, A.P., Dietzel, M., Fichtner, V., Fischer, C., Hippler, D., Leis, A.,
639 Baldermann, C., Mavromatis, V., Stickler, C.P., Strauss, H., 2015. The role of bacterial
640 sulfate reduction during dolomite precipitation: Implications from Upper Jurassic platform
641 carbonates. *Chemical Geology* 412, 1-14.

642 Baldermann, A., Warr, L.N., Grathoff, G.H., Dietzel, M., 2013. The rate and mechanism of
643 deep-sea glauconite formation at the ivory coast–ghana marginal ridge. *Clays and Clay
644 Minerals* 61, 258-276.

645 Banerjee, S., Bansal, U., Vilas Thorat, A., 2016. A review on palaeogeographic implications
646 and temporal variation in glaucony composition. *Journal of Palaeogeography* 5, 43-71.

647 Barbetti, M., Taborin, Y., Schmider, B., Flude, K., 1980. Archaeomagnetic results from late
648 Pleistocene hearths at Etiolles and Marsangy, France. *Archaeometry* 22, 25-46.

649 Bleil, U., Von Dobeneck, T., 1999. Geomagnetic events and relative paleointensity records—
650 Clues to high-resolution paleomagnetic chronostratigraphies of Late Quaternary marine
651 sediments?, *Use of proxies in paleoceanography*. Springer, pp. 635-654.

652 Böhm, E., Lippold, J., Gutjahr, M., Frank, M., Blaser, P., Antz, B., Fohlmeister, J., Frank, N.,
653 Andersen, M., Deininger, M., 2015. Strong and deep Atlantic meridional overturning
654 circulation during the last glacial cycle. *Nature* 517, 73-76.

655 Bonhommet, N., Babkine, J., 1967. Sur la presence d'aimantations inversees dans la Chaine
656 des Puys. *Comptes rendus hebdomadaires des seances de l'academie des sciences serie b* 264,
657 92-94.

658 Chafetz, H.S., Reid, A., 2000. Syndepositional shallow-water precipitation of glauconitic
659 minerals. *Sedimentary Geology* 136, 29-42.

660 Curry, W.B., Oppo, D.W., 2005. Glacial water mass geometry and the distribution of $\delta^{13}\text{C}$ of
661 ΣCO_2 in the western Atlantic Ocean. *Paleoceanography* 20.

662 Faugères, J.-C., Gonthier, E., Stow, D.A.V., 1984. Contourite drift molded by deep
663 Mediterranean outflow. *Geology* 12, 296-300.

664 Faugères, J.-C., Zaragosi, S., Mézerais, M., Massé, L., 2002. The Vema contourite fan in the
665 South Brazilian basin. *Geological Society, London, Memoirs* 22, 209-222.

666 Faugères, J.C., Mulder, T., 2011. Contour Currents and Contourite Drifts. in: Heiko Hüneke
667 and Thierry Mulder, *Deep sea sediments, elsevier publications, developments in
668 sedimentology* 63, 149-205.

669 Gaudin, A., Buatier, M., Beaufort, D., Petit, S., Grauby, O., Decarreau, A., 2005.
670 Characterization and origin of Fe^{3+} -montmorillonite in deep-water calcareous sediments
671 (Pacific Ocean, Costa Rica margin). *Clays and Clay Minerals* 53, 452-465.

672 Gaullier, V., Loncke, L., Droz, L., Basile, C., Maillard, A., Patriat, M., Roest, W.R.,
673 Loubrieu, B., Folens, L., Carol, F., 2010. Slope instability on the French Guiana transform
674 margin from swath-bathymetry and 3.5 kHz echograms, *Submarine Mass Movements and
675 Their Consequences*. Springer, pp. 569-579.

676 Gibbard, P., Cohen, K.M., 2008. Global chronostratigraphical correlation table for the last 2.7
677 million years. *Episodes* 31, 243-247.

678 Giresse, P., 2008. Chapter 12 Some Aspects of Diagenesis in Contourites, In: Rebesco, M.,
679 Camerlenghi, A. (Eds.), *Developments in Sedimentology*. Elsevier, pp. 203-221.

680 Giresse, P., Wiewióra, A., 2001. Stratigraphic condensed deposition and diagenetic evolution
681 of green clay minerals in deep water sediments on the Ivory Coast–Ghana Ridge. *Marine
682 Geology* 179, 51-70.

683 Gonthier, E., Faugères, J.C., Stow, D.A.V., 1984. Contourite facies of the Faro drift.
684 *Geological society of London, special publication* 15, 275-292.

685 Guillou, H., Singer, B.S., Laj, C., Kissel, C., Scaillet, S., Jicha, B.R., 2004. On the age of the
686 Laschamp geomagnetic excursion. *Earth and Planetary Science Letters* 227, 331-343.

687 Heezen, B.C., 1959. Dynamic Processes of Abyssal Sedimentation: Erosion, Transportation,
688 and Redeposition on the Deep-sea floor. *Geophysical Journal International* 2, 142-163.

689 Heezen, B.C., Hollister, C., 1964. Deep-sea current evidence from abyssal sediments. *Marine*
690 *Geology* 1, 141-174.

691 Heezen, B.C., Johnson, G.L., 1963. A moated knoll in the Canary Passage. *Dent. Hydrograph.*
692 *Z.* 16, 269-272.

693 Hernández-Molina, F.J., Paterlini, M., Violante, R., Marshall, P., de Isasi, M., Somoza, L.,
694 Rebesco, M., 2009. Contourite depositional system on the Argentine Slope: An exceptional
695 record of the influence of Antarctic water masses. *Geology* 37, 507-510.

696 Hurley, P., Rand, J., Pinson, W., Fairbairn, H., de Almeida, F., Melcher, G., Cordani, U.,
697 Kawashita, K., Vadoros, P., 1967. Test of Continental Drift by Comparison of Radiometric
698 Ages A pre-drift reconstruction shows matching geologic age provinces in West Africa and
699 Northern Brazil. *Science* 157, 495-500.

700 Ingram, W.C., 2006. Anatomy of Oligocene-Miocene debris flow and slumps form Demerara
701 Rise: implications for margin destruction American Association of Petroleum Geologists
702 2006 annual Convention, Houston.

703 Ingram, W.C., Mosher, D.C., Wise, S.W.J., 2011. Biostratigraphy of an upper Miocene mass
704 transport deposit on Demerara Rise, northern South American margin, In: Shipp, C., Weimer,
705 P., Posamentier, H. (Eds.), *Mass-transport Deposits in Deepwater Settings*. SEPM Special
706 Publication 96, pp. 457-498.

707 Kageyama, M., Merkel, U., Otto-Bliesner, B., Prange, M., Abe-Ouchi, A., Lohmann, G.,
708 Ohgaito, R., Roche, D., Singarayer, J., Swingedouw, D., 2013. Climatic impacts of fresh
709 water hosing under Last Glacial Maximum conditions: a multi-model study. *Climate of the*
710 *Past* 9, 935-953.

711 Lee, S.H., Bahk, J.J., Chough, S.K., Back, G.G., Yoo, H.S., 2004. Late Quaternary
712 sedimentation in the Ulleung Interplain Gap, East Sea (Korea). *Marine Geology* 206, 225-
713 248.

714 Lippold, J., Gutjahr, M., Blaser, P., Christner, E., de Carvalho Ferreira, M.L., Mulitza, S.,
715 Christl, M., Wombacher, F., Böhm, E., Antz, B., 2016. Deep water provenance and dynamics
716 of the (de) glacial Atlantic meridional overturning circulation. *Earth and Planetary Science*
717 *Letters* 445, 68-78.

718 Lisiecki, L.E., Raymo, M.E., 2005. A Pliocene-Pleistocene stack of 57 globally distributed
719 benthic $\delta^{18}\text{O}$ records. *Paleoceanography* 20.

720 Lisiecki, L.E., Raymo, M.E., 2009. Diachronous benthic $\delta^{18}\text{O}$ responses during late
721 Pleistocene terminations. *Paleoceanography*.

722 Loncke, L., Droz, L., Gaullier, V., Basile, C., Patriat, M., Roest, W., 2009. Slope instabilities
723 from echo-character mapping along the French Guiana transform margin and Demerara
724 abyssal plain. *Marine and Petroleum Geology* 26, 711-723.

725 Loncke, L., Maillard, A., Basile, C., Roest, W.R., Bayon, G., Gaullier, V., Pattier, F., Mercier
726 de Lépinay, M., Grall, C., Droz, L., Marsset, T., Giresse, P., Caprais, J.C., Cathalot, C.,
727 Graindorge, D., Heuret, A., Lebrun, J.F., Bermell, S., Marcaillou, B., Sotin, C., Hebert, B.,
728 Patriat, M., Bassetti, M.A., Tallobre, C., Buscail, R., Durrieu de Madron, X., Bourrin, F.,
729 2016. Structure of the Demerara passive-transform margin and associated sedimentary
730 processes. Initial results from the IGUANES cruise. Geological Society, London, Special
731 Publications 431.

732 Lopes, R.P., Kinoshita, A., Baffa, O., Figueiredo, A.M.G., Dillenburg, S.R., Schultz, C.L.,
733 Pereira, J.C., 2014. ESR dating of Pleistocene mammals and marine shells from the coastal
734 plain of Rio Grande do Sul state, southern Brazil. *Quaternary International* 352, 124-134.

735 López-Otálvaro, G.-E., Flores, J., Sierro, F., Cacho, I., Grimalt, J.-O., Michel, E., Cortijo, E.,
736 Labeyrie, L., 2009. Late Pleistocene palaeoproductivity patterns during the last climatic cycle
737 in the Guyana Basin as revealed by calcareous nannoplankton. *EEarth* 4, 1-13.

738 Lund, S.P., Schwartz, M., Keigwin, L., Redefinition of the Blake Event.

739 Maley, J., Livingstone, D.A., Giresse, P., Thouveny, N., Brenac, P., Kelts, K., Kling, G.,
740 Stager, C., Haag, M., Fournier, M., Bandet, Y., Williamson, D., Zogning, A., 1990.
741 Lithostratigraphy, volcanism, paleomagnetism and palynology of Quaternary lacustrine
742 deposits from Barombi Mbo (West Cameroon): Preliminary results. *Journal of Volcanology
743 and Geothermal Research* 42, 319-335.

744 McCave, I., Manighetti, B., Robinson, S., 1995. Sortable silt and fine sediment
745 size/composition slicing: parameters for palaeocurrent speed and palaeoceanography.
746 *Paleoceanography* 10, 593-610.

747 McCave, I.N., Hall, I.R., 2006. Size sorting in marine muds: Processes, pitfalls, and prospects
748 for paleoflow-speed proxies. *Geochemistry, Geophysics, Geosystems* 7, 1-37.

749 McRae, S.G., 1972. Glauconite. *Earth-Science Reviews* 8, 397-440.

750 Meniel, L., Timmermann, A., Friedrich, T., England, M., 2014. Hindcasting the continuum
751 of Dansgaard–Oeschger variability: mechanisms, patterns and timing. *Climate of the Past* 10,
752 63-77.

753 Mercier de Lépinay, M., Loncke, L., Basile, C., Roest, W., Patriat, M., Maillard, A., De
754 Clarens, P., 2016. Transform continental margins - Part 2: A worldwide inventory.
755 *Tectonophysics*.

756 Mörner, N.-A., 1977. The Gothenburg Magnetic Excursion. *Quaternary Research* 7, 413-427.

757 Mörner, N.-A., 1986. Geomagnetic excursions in late Brunhes time, European long-core data.
758 *Physics of the Earth and Planetary Interiors* 44, 47-52.

759 Mosblech, N.A., Bush, M.B., Gosling, W.D., Hodell, D., Thomas, L., van Calsteren, P.,
760 Correa-Metrio, A., Valencia, B.G., Curtis, J., van Woesik, R., 2012. North Atlantic forcing of
761 Amazonian precipitation during the last ice age. *Nature Geoscience* 5, 817-820.

762 Müller-Karger, F., McClain, C., Fisher, T., Esaias, W., Varela, R., 1989. Pigment distribution
763 in the Caribbean Sea: Observations from space. *Progress in Oceanography* 23, 23-64.

764 Nace, T.E., Baker, P.A., Dwyer, G.S., Silva, C.G., Rigsby, C.A., Burns, S.J., Giosan, L., Otto-
765 Bliessner, B., Liu, Z., Zhu, J., 2014. The role of North Brazil Current transport in the
766 paleoclimate of the Brazilian Nordeste margin and paleoceanography of the western tropical
767 Atlantic during the late Quaternary. *Palaeogeography, Palaeoclimatology, Palaeoecology* 415,
768 3-13.

769 Odin, G., Fullagar, P., 1988. Chapter C4 geological significance of the glaucony facies.
770 *Developments in sedimentology* 45, 295-332.

771 Odin, G.S., 1988. *Green Marine Clays*. Elsevier.

772 Pattier, F., Loncke, L., Gaullier, V., Basile, C., Maillard, A., Imbert, P., Roest, W.R.,
773 Vendeville, B.C., Patriat, M., Loubrieu, B., 2013. Mass-transport deposits and fluid venting in
774 a transform margin setting, the eastern Demerara Plateau (French Guiana). *Marine and
775 Petroleum Geology* 46, 287-303.

776 Pattier, F., Loncke, L., Imbert, P., Gaullier, V., Basile, C., Maillard, A., Roest, W.R., Patriat,
777 M., Vendeville, B.C., 2015. Origin of an enigmatic regional Mio-Pliocene unconformity on
778 the Demerara plateau. *Marine Geology* 365, 21-35.

779 Plenier, G., Valet, J.-P., Guérin, G., Lefèvre, J.-C., LeGoff, M., Carter-Stiglitz, B., 2007.
780 Origin and age of the directions recorded during the Laschamp event in the Chaîne des Puys
781 (France). *Earth and Planetary Science Letters* 259, 414-431.

782 Rama-Corredor, O., Martrat, B., Grimalt, J.O., López-Otalvaro, G.E., Flores, J.A., Sierro, F.,
783 2015. Parallelisms between sea surface temperature changes in the western tropical Atlantic
784 (Guiana Basin) and high latitude climate signals over the last 140 000 years. *Climate of the*
785 *Past* 11, 1297-1311.

786 Rebesco, M., Camerlenghi, A., 2008. *Contourites*. Elsevier.

787 Rebesco, M., Hernández-Molina, F.J., Van Rooij, D., Wåhlin, A., 2014. Contourites and
788 associated sediments controlled by deep-water circulation processes: State-of-the-art and
789 future considerations. *Marine Geology* 352, 111-154.

790 Reimer, P., Bard, E., Bayliss, A., Beck, J., Blackwell, P., Bronk Ramsey, C., Buck, C.,
791 Cheng, H., Edwards, R., Friedrich, M., Grootes, P., Guilderson, T., Haflidason, H., Hajdas, I.,
792 Hatté, C., Heaton, T., Hogg, A., Hughen, K., Kaiser, K., Kromer, B., Manning, S., Niu, M.,
793 Reimer, R., Richards, D., Scott, E., Southon, J., Turney, C., van der Plicht, J., 2013. IntCal13
794 and MARINE13 radiocarbon age calibration curves 0-50000 years calBP *Radiocarbon* 55(4).

795 Shackleton, N.J., Sánchez-Goñi, M.F., Pailler, D., Lancelot, Y., 2003. Marine Isotope
796 Substage 5e and the Eemian Interglacial. *Global and Planetary Change* 36, 151-155.

797 Shanmugam, G., 2016. The contourite problem. *Sediment Provenance*.

798 Smith, G., Creer, K.M., 1986. Analysis of geomagnetic secular variations 10 000 to 30 000
799 years bp, Lac du Bouchet, France. *Physics of the Earth and Planetary Interiors* 44, 1-14.

800 Smith, J.D., Foster, J.H., 1969. Geomagnetic reversal in Brunhes normal polarity epoch.
801 *Science* 163, 565-567.

802 Stow, D., Faugères, J.-C., 2008a. Contourite facies and the facies model. *Developments in*
803 *Sedimentology* 60, 223-256.

804 Stow, D.A.V., Faugères, J.-C., Howe, J.A., Pudsey, C.J., Viana, A.R., 2002. Bottom currents,
805 contourites and deep-sea sediment drifts: current state-of-the-art. Bottom currents, contourites
806 and deep-sea sediment drifts: current state-of-the-art. In: Stow, D.A.V., Pudsey, C.J., Howe,
807 J.A., Faugères, J.-C., Viana, A.R. (Eds.), *Deep-Water Contourite Systems: Modern Drifts and*
808 *Ancient Series, Seismic and Sedimentary Characteristics: Geological Society London Memoir*
809 *22*, 137-154.

810 Stow, D.A.V., Faugères, J.C., 2008b. Chapter 13 Contourite Facies and the Facies Model, In:
811 Rebesco, M., Camerlenghi, A. (Eds.), *Developments in Sedimentology*. Elsevier, pp. 223-256.

812 Tallobre, C., 2017. Mise en évidence d'un système de dépôt contouritique et des processus
813 sédimentaires associés sur le plateau de Demerara (marge guyanaise), Cefrem. Université de
814 Perpignan via Domitia, Perpignan.

815 Tallobre, C., Loncke, L., Bassetti, M.-A., Giresse, P., Bayon, G., Buscail, R., de Madron,
816 X.D., Bourrin, F., Vanhaesebroucke, M., Sotin, C., 2016. Description of a contourite
817 depositional system on the Demerara Plateau: Results from geophysical data and sediment
818 cores. *Marine Geology* 378, 56-73.

819 Thouveny, N., Williamson, D., 1988. Palaeomagnetic study of the Holocene and Upper
820 Pleistocene sediments from Lake Barombi Mbo, Cameroun: first results. *Physics of the Earth*
821 *and Planetary Interiors* 52, 193-206.

822 Tudryn, A., Tucholka, P., Gibert, E., Gasse, F., Wei, K., 2010. A late Pleistocene and
823 Holocene mineral magnetic record from sediments of Lake Aibi, Dzungarian Basin, NW
824 China. *Journal of Paleolimnology* 44, 109-121.

- 825 van der Hammen, T., Absy, M.L., 1994. Pollen and Climate Amazonia during the last glacial.
826 *Palaeogeography, Palaeoclimatology, Palaeoecology* 109, 247-261.
- 827 Viana, A.R., Faugeres, J.C., Kowsmann, R.O., Lima, J.A.M., Caddah, L.F.G., Rizzo, J.G.,
828 1998. Hydrology, morphology and sedimentology of the Campos continental margin, offshore
829 Brazil. *Sedimentary Geology* 115, 133-157.
- 830 Wiewióra, A., Giresse, P., Petit, S., Wilamowski, A., 2001. A deep-water glauconitization
831 process on the Ivory Coast–Ghana marginal ridge (ODP site 959): determination of Fe³⁺-rich
832 montmorillonite in green grains. *Clays and Clay Minerals* 49, 540-558.
- 833 Zaragosi, S., Bourillet, J.-F., Eynaud, F., Toucanne, S., Denhard, B., Van Toer, A., Lanfumey,
834 V., 2006. The impact of the last European deglaciation on the deep-sea turbidite systems of
835 the Celtic-Armorican margin (Bay of Biscay). *Geo-Marine Letters* 26, 317-329.
- 836

837 Table 1: Radiocarbon dates for well-preserved *Globigerinoides* sp. fractions from samples
838 collected from core IG-KSF-11. The calibrated ages were calculated using Calib 7.0.4 with
839 the Marine 09 calibration curve (Reimer et al., 2013).

840 Table 2: Tie points identified in the IG-KSF-05 and IG-KSF-11 core based on correlation
841 with reference oxygen isotope curves (Martinson et al., 1987; Walker et al., 2009)

842 Table 3: Sedimentary facies table based on the description of core, microscopic observation
843 (sand fraction and thin section).

844 Table 4: Average chemical composition measured by microprobe coupled to the SEM on mud
845 and on green grains coming from the core IG-KSF-11 at different depth on the core (0 cm, 60
846 cm, 70 cm, 90 cm, 300 cm, 420 cm, 442 cm, 460 cm, 590 cm). For each grain, 2 measures
847 was performed, results the average is established in function of the grain colour (yellowish-
848 green, green, and dark green, the last one being sub-divided into dark and very dark green).

849 Figure 1: General map and location of the study area with position of North Atlantic Deep
850 water (NADW) and Antarctic Bottom Water (AABW).

851 Figure 2: Bathymetric map with the position of cores analysed in this paper. The core IG-
852 KSF-05 was collected inside the drift of the Demerara Contourite Depositional System (CDS)
853 whereas the core IG-KSF-11 and IG-KSF-15 were collected inside the moat of this CDS.

854 Figure 3: Sedimentary log of core IG-KSF-05, collected in the sedimentary drift, presenting
855 the identified sedimentary facies (more details about facies in table 3), the planktic
856 (*Globigerina ruber*) and benthic (*Uvigerina mediterranea*) oxygen isotope records, the
857 palaeomagnetism record (NRM, inclination and declination), glauconitic grain concentration
858 on bulk sediment (total green grains with the green curve) and Ca XRF record.

859 Figure 4: Sedimentary log of core IG-KSF-11, collected in the contouritic moat, illustrating
860 the identified sedimentary facies (more details about facies in table 3), planktic (*Globigerina*

861 ruber) and benthic (*Uvigerina mediterranea*) oxygen isotope record, the palaeomagnetism
862 record (NRM, inclination and declination), glauconitic grain quantification on bulk sediment
863 (total green grains with the green curve, and the bars represent the relative content in function
864 of the greening (yellowish, green and dark green grains), the sortable silt on the free-
865 carbonated record and Ca XRF record.

866 Figure 5: Sedimentary log of core IG-KSF-15, collected in the moat, with glauconitic grain
867 quantitative estimation on bulk sediment (total green grains with the green curve) and Ca
868 XRF record.

869 Figure 6: Reference isotopic curves of Guyana (López-Otálvaro et al., 2009), a global curve
870 for the Atlantic domain (Lisiecki and Raymo, 2005; Lisiecki and Raymo, 2009; Lopes et al.,
871 2014), North Brazil (Arz et al., 1998), and IGUANES data for cores IG-KSF-05 and IG-KSF-
872 11.

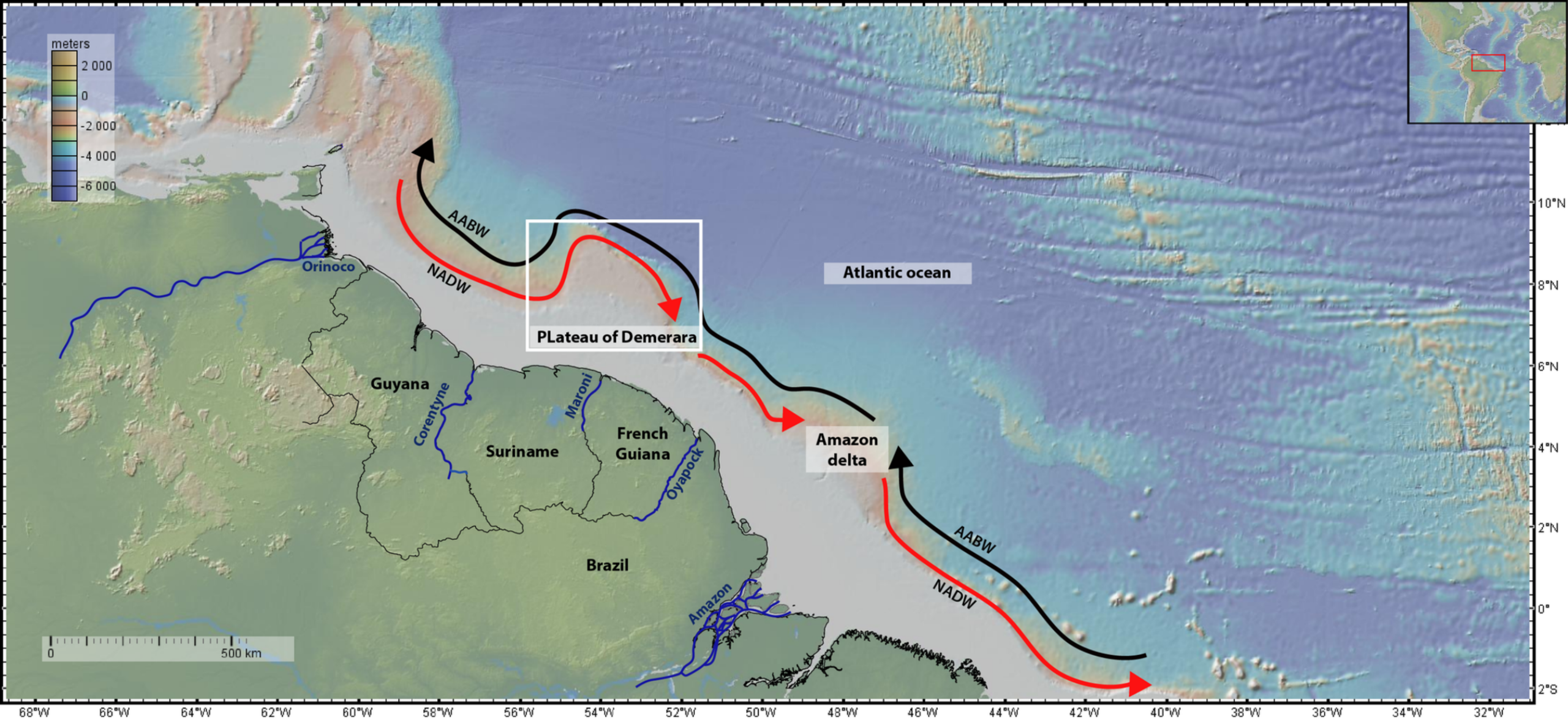
873 Figure 7: Thin section photos illustrating the different micro-facies F2 to F7 (see table 3).

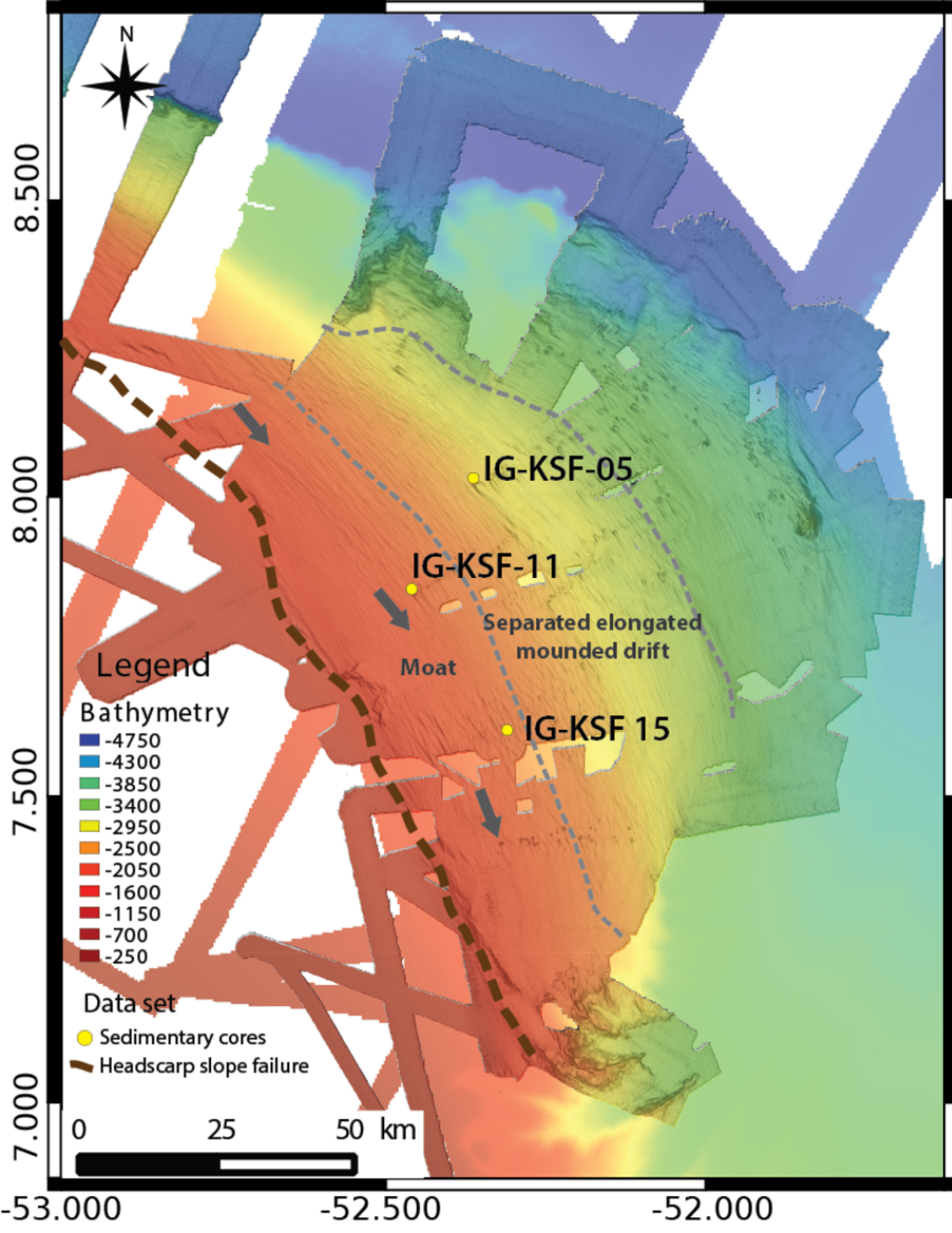
874 Figure 8: Thin section s of some sediment facies. (F: foraminifera, G.If: glauconitic infilling,
875 Gic: glauconitic intraclast, GM: glauconitic mould, Qz: quartz)

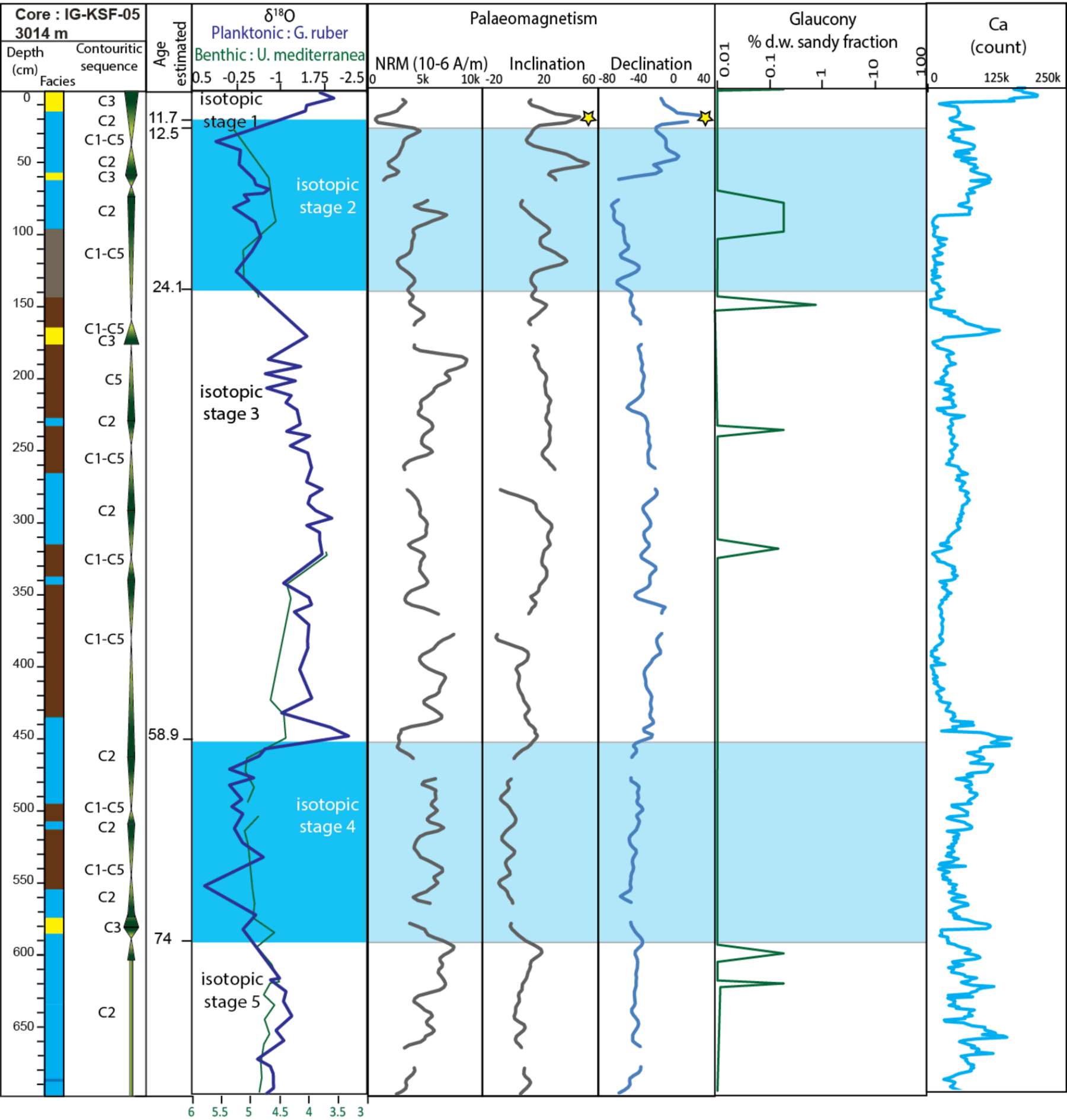
876 Figure 9: Illustration of the degree of glauconitic maturity. The different degrees of maturity
877 are illustrated by the colour of grains, the structure at the grain surface with MEB picture, the
878 micro-structure with MEB picture, and the elementary composition measured by microprobe
879 which is one-time the on the single related grain.

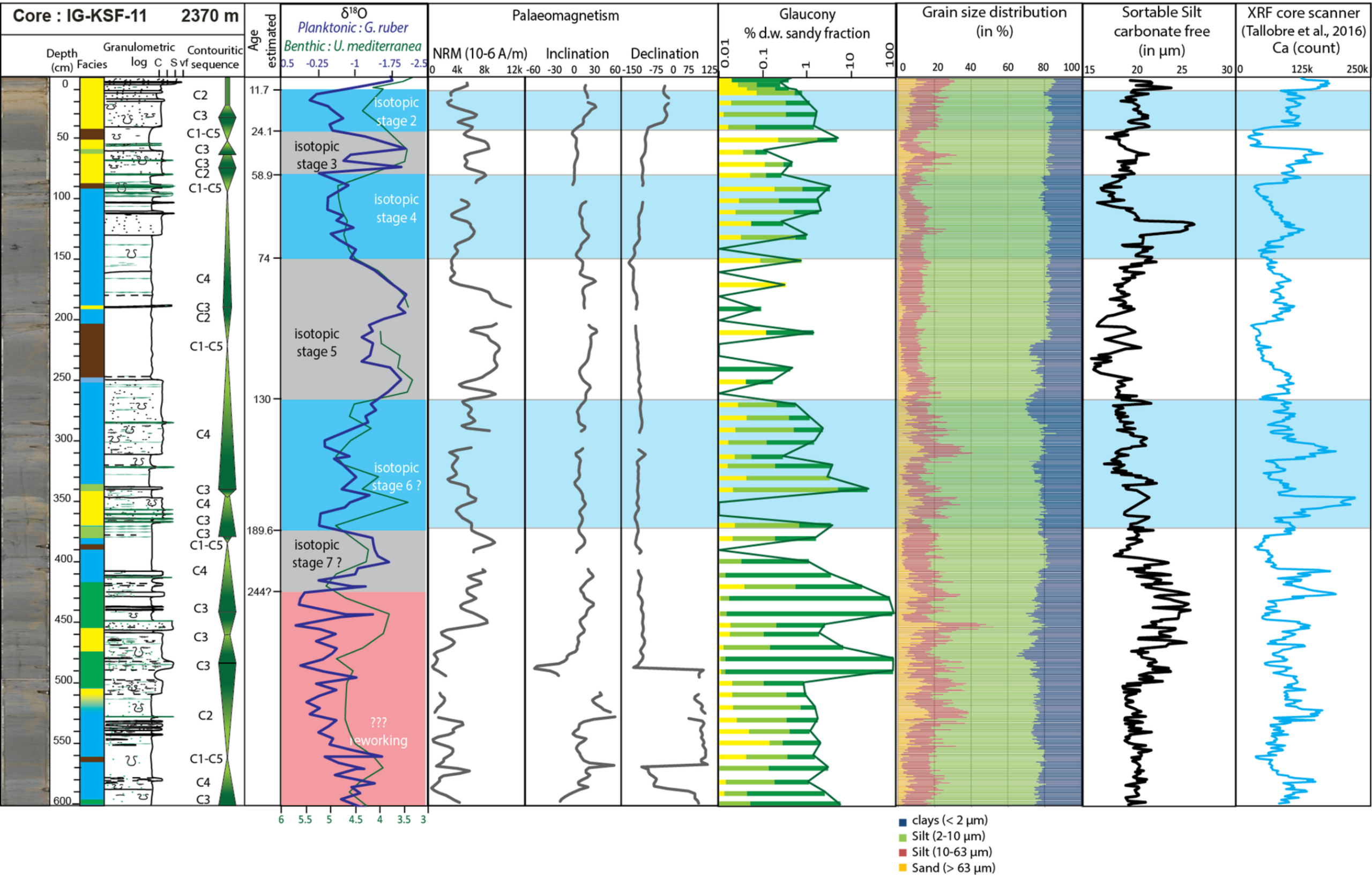
880 Figure 10: Schematic evolution of glauconitic grains from pristine marine mud to dark green
881 grains with the mean elementary composition measured by microprobe and established for
882 each class colour with the two values on each grain.

883 Figure 11: Schema of the ideal contouritic sequence (modified from (Stow and Faugères
884 (2008a)) and according to the glauconitisation processes. The concentration and the
885 mineralogic maturity of the green grains increase with the winnowing intensity.









Core : IG-KSF-15
2578 m

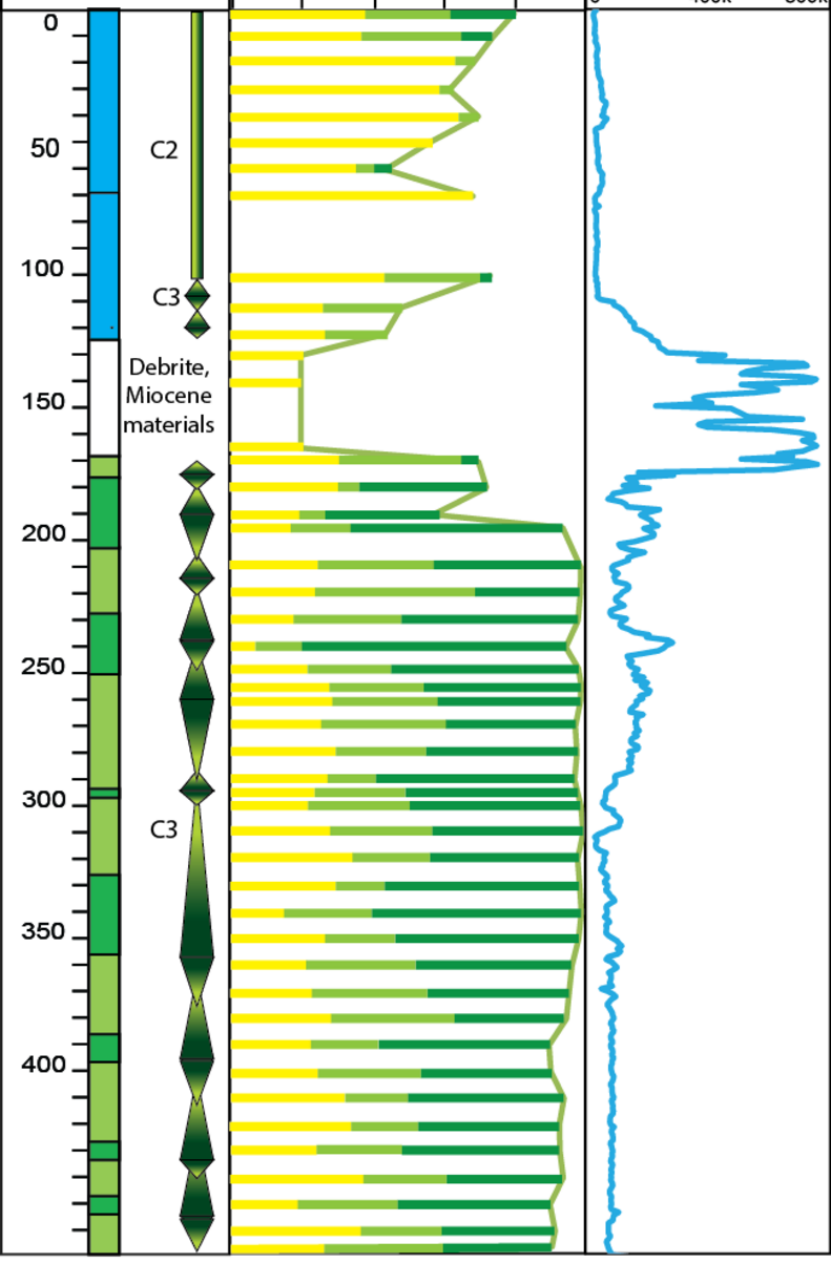
Depth (cm) Contouritic
sequence
Facies

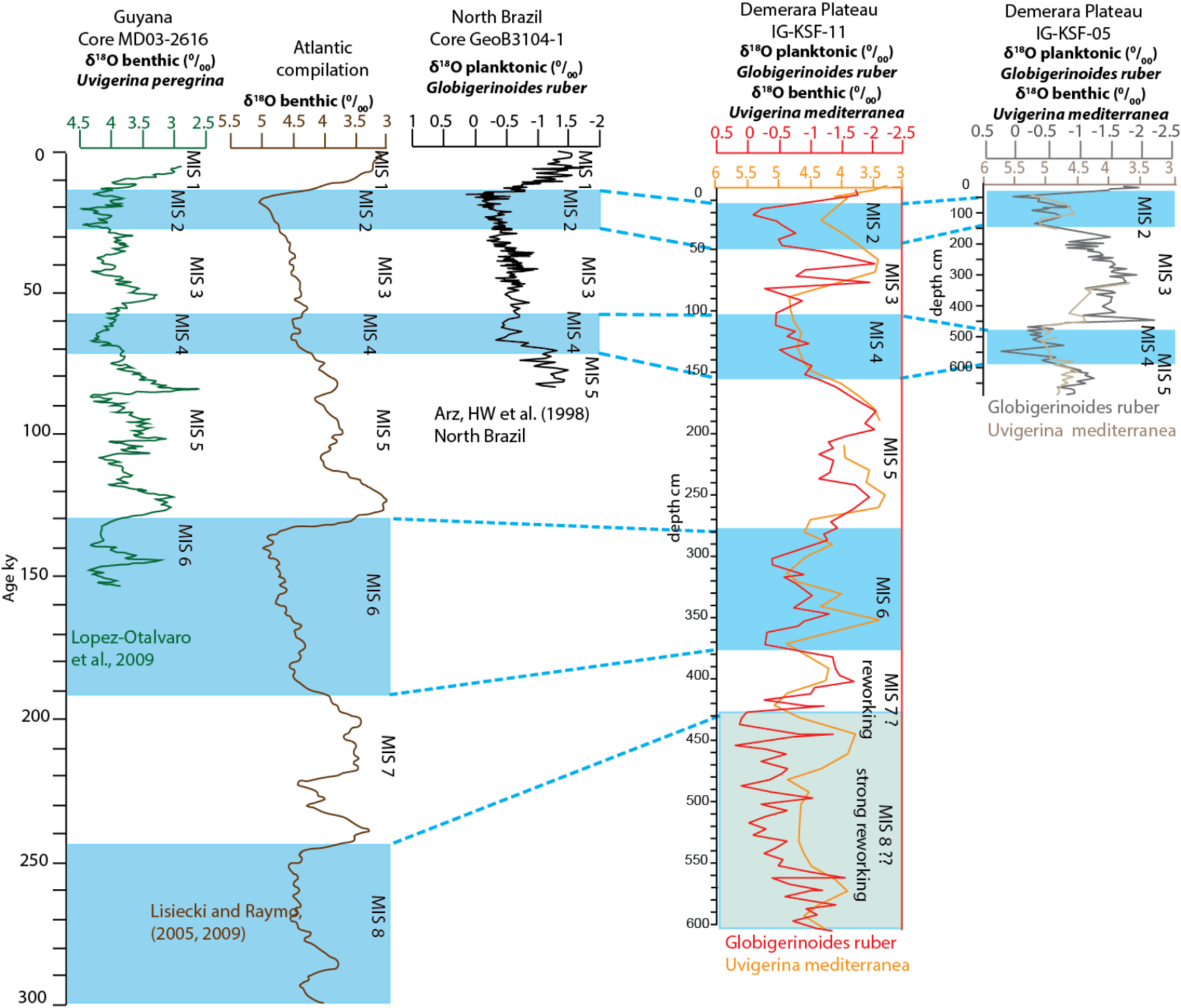
Glaucony
% d.w. sandy fraction

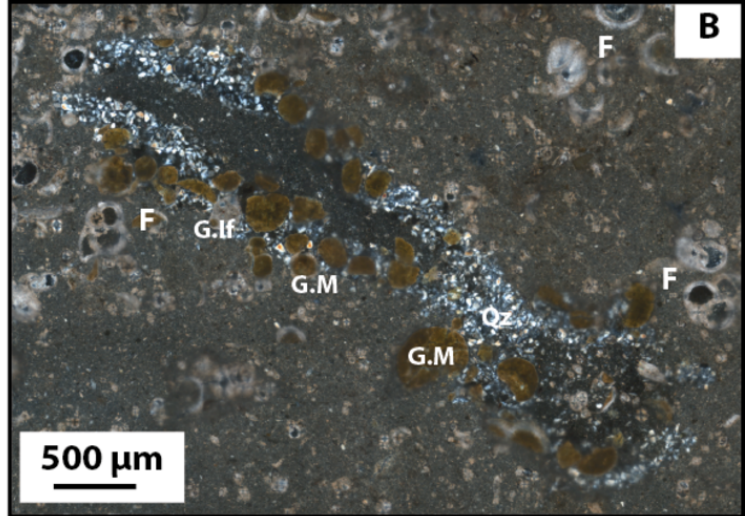
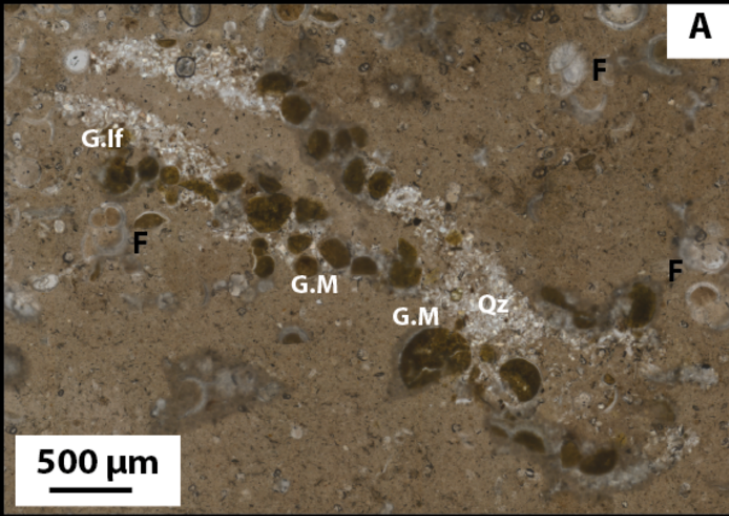
0.001 0.01 0.1 1 10

Ca
(count)

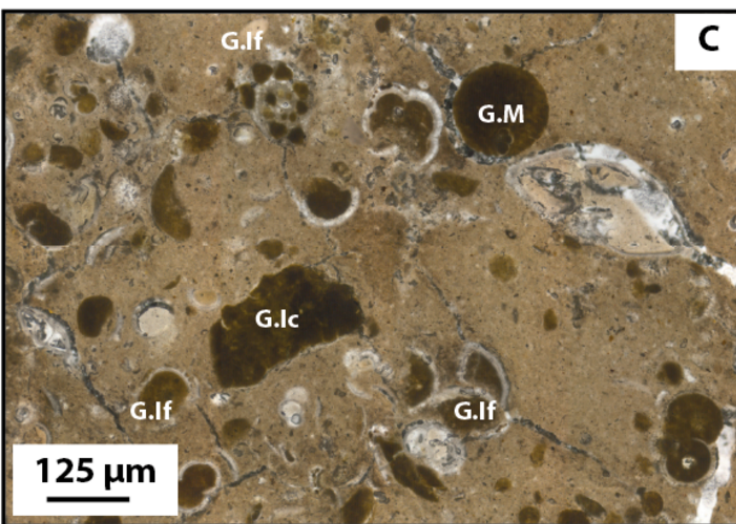
0 400k 800k



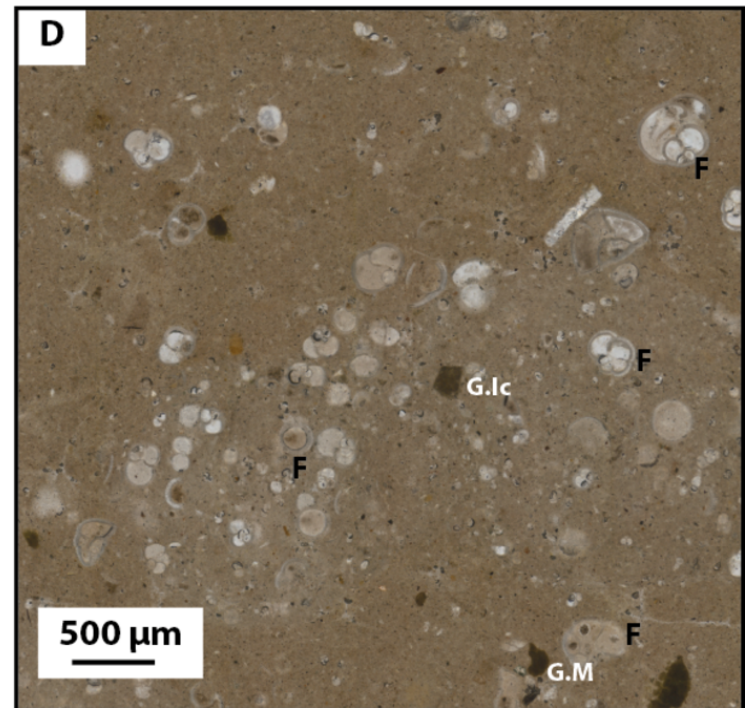




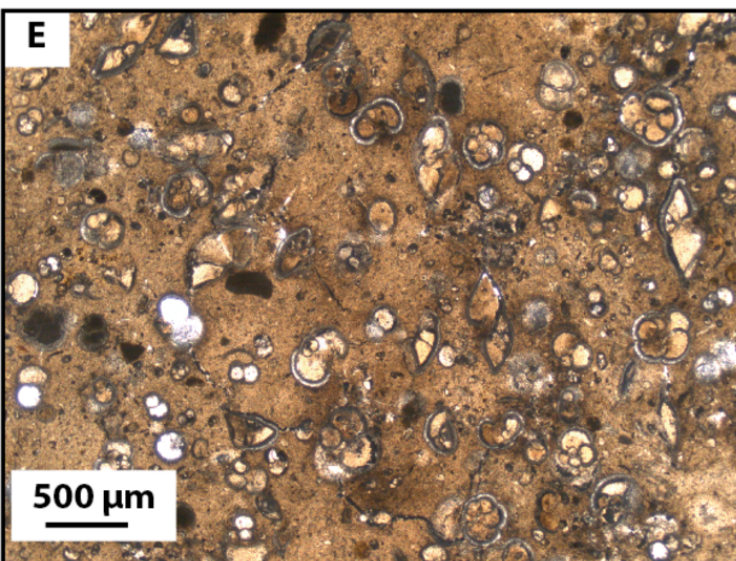
(A) in LPNA and (B) in LPA photos, illustration of bioturbation rich in glaucony and quartz in a facies F4.



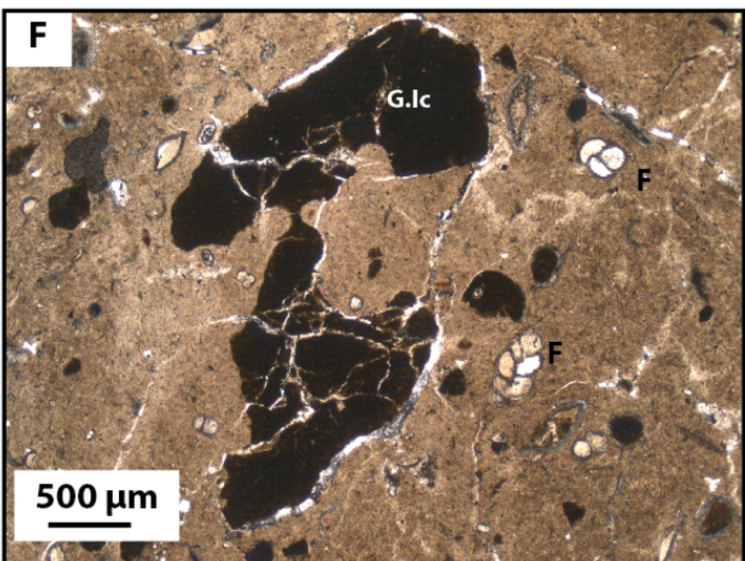
(C) LPNA photo, facies F2 with the different type of glaucony grains: inside foraminifera test, with foraminifera shape without test, and clast. Grains show a high degree of fracturing.



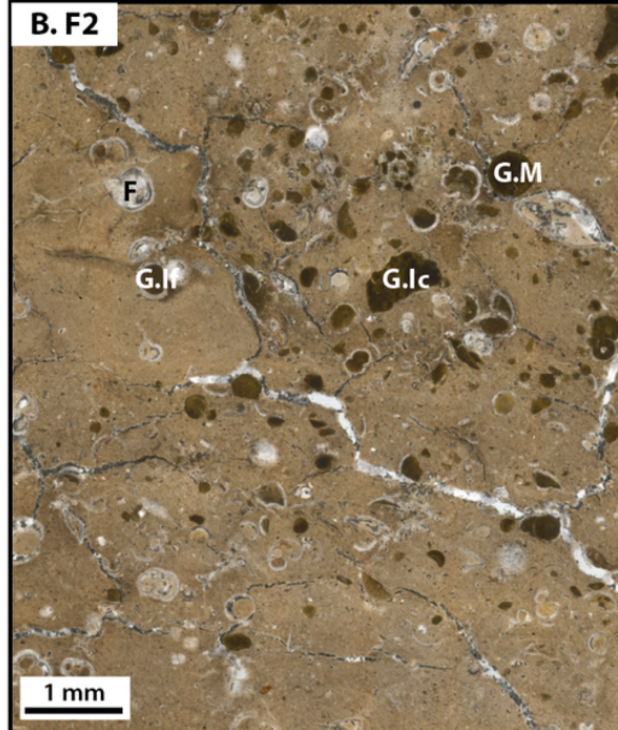
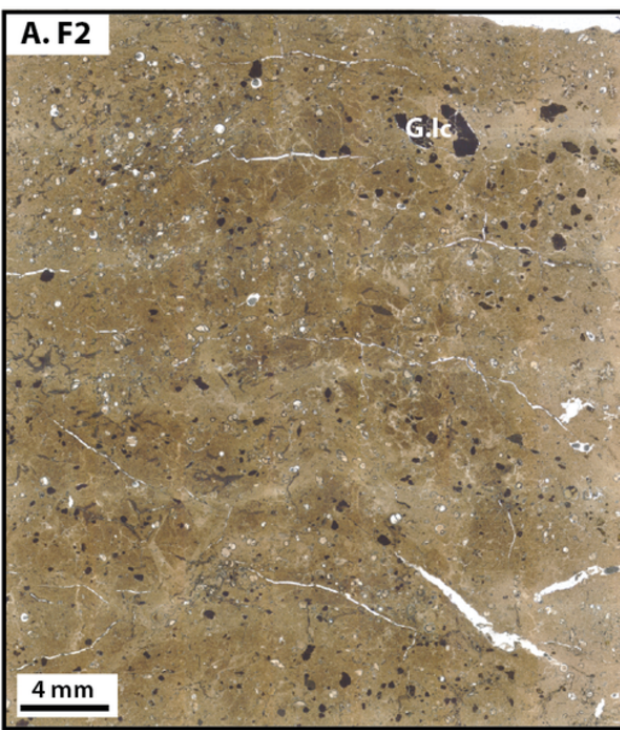
(D) LPNA photo F4, illustrated a bioturbation rich in foraminifera forming a lense in a fine mud with some grains.



(E) LPNA photo of F3, sandy foraminifera with some glaucony grains (around 10% of glaucony), low fracturing.



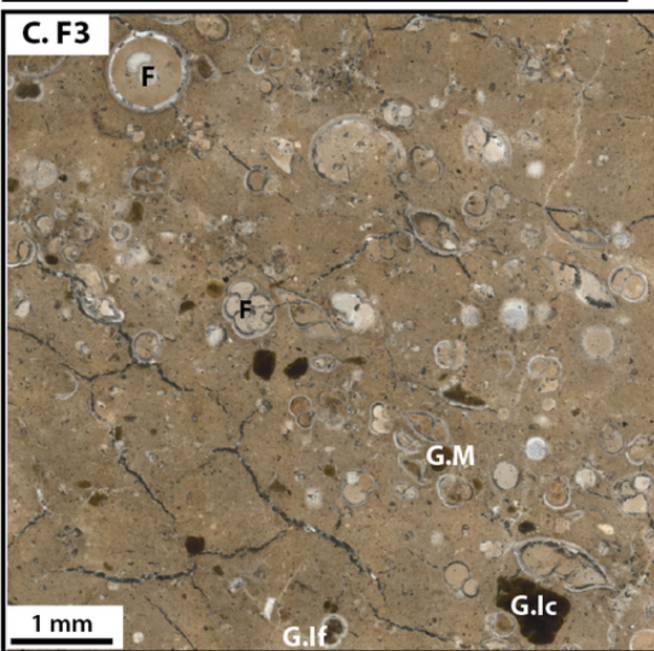
(F) LPNA photo of a glaucony clast probably coming from a glauconitic lithified surface.



(A) and (B) Facies F2, glauconitic rich (*Glc*) and foraminifera rich (*F*). Glauconitic grains are present inside foraminifera test (*G.lf*), foraminifera moulding (*G.M*) or in intraclast (*G.lc*).

(C) Facies F3, sandy facies foraminifera rich (*F*) and glauconitic rich (*Glc*). See laminae rich in sandy grains.

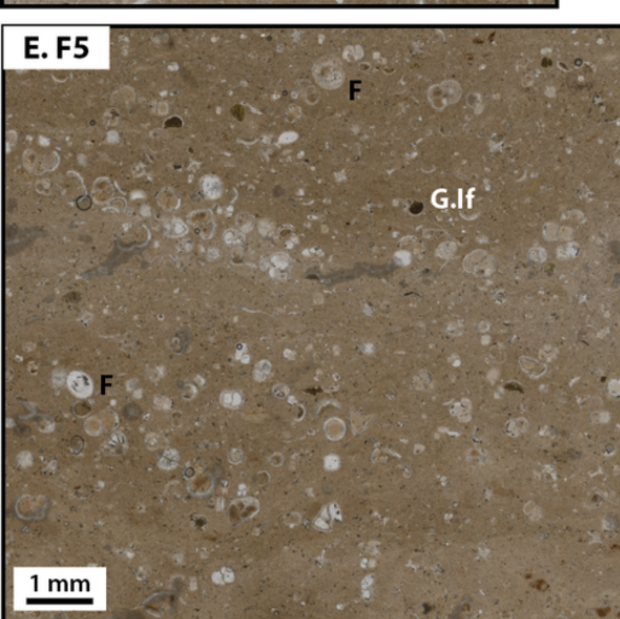
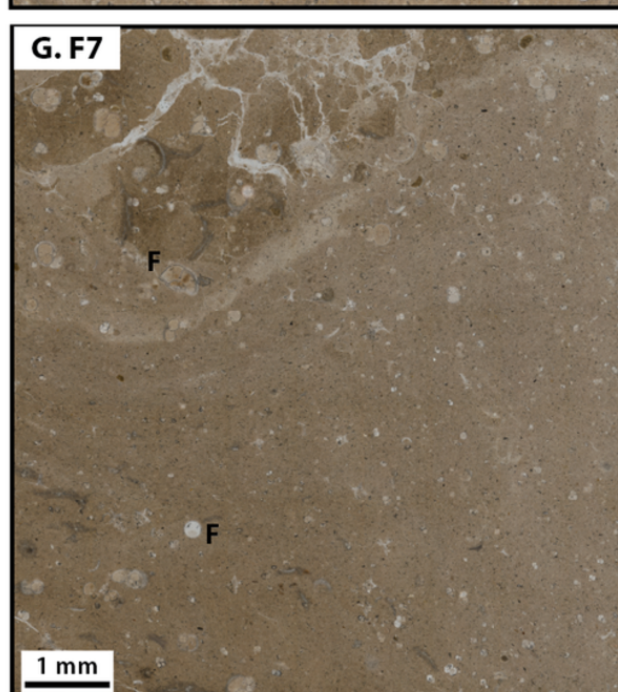
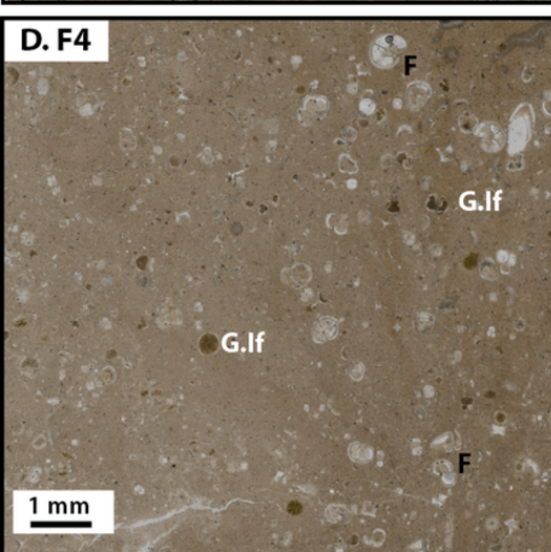
(D) Facies F4 foraminifera- and glauconitic- bearing muddy facies, moderately rich in foraminifera (*F*) with few glauconitic grains inside foraminifera (*G.lf*).

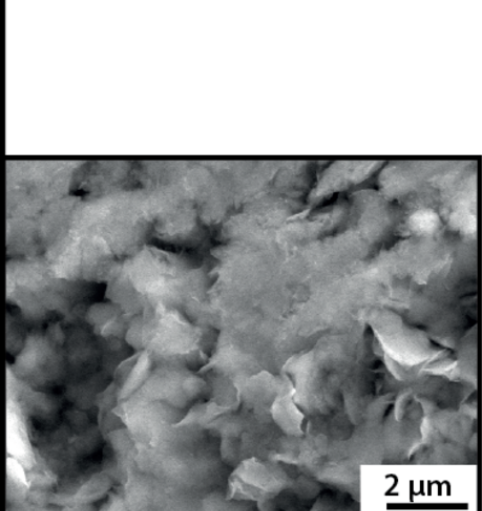
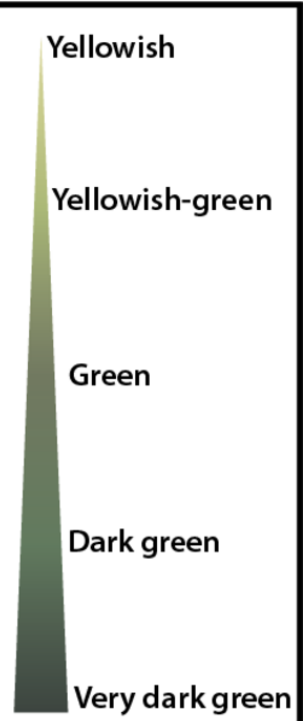
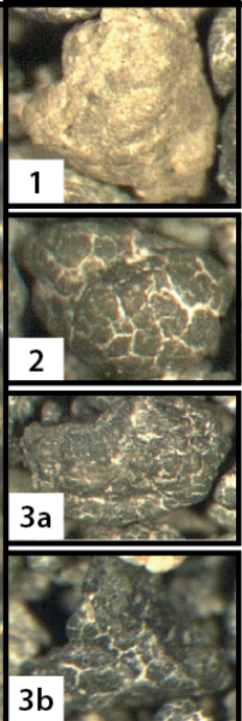
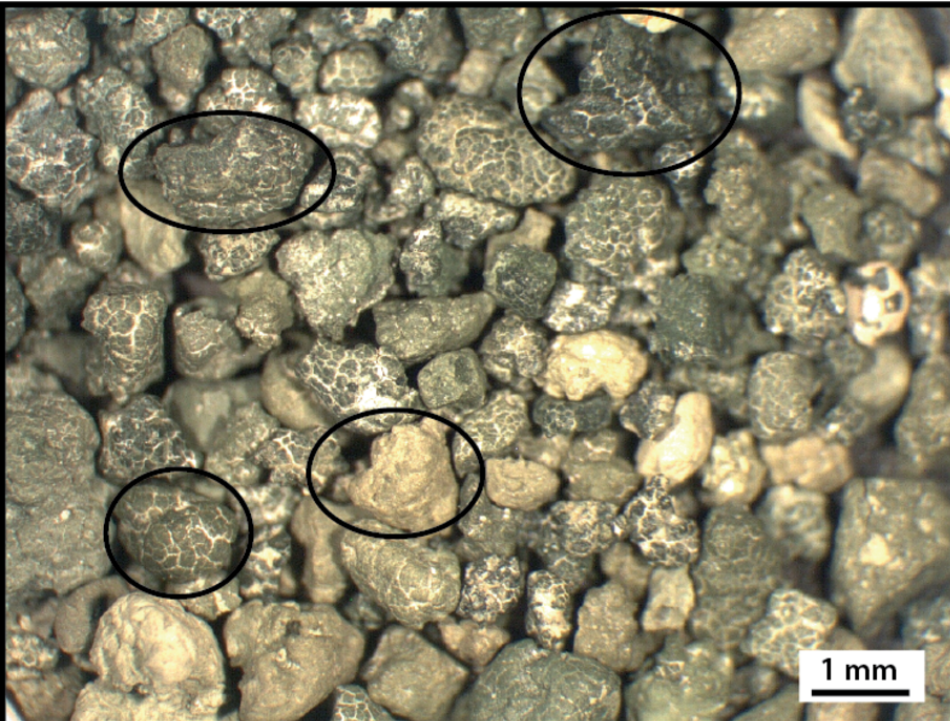


(E) Facies F5, foraminifera sand rich in foraminifera (*F*) and poor in glauconitic grains with laminae rich in foraminifera.

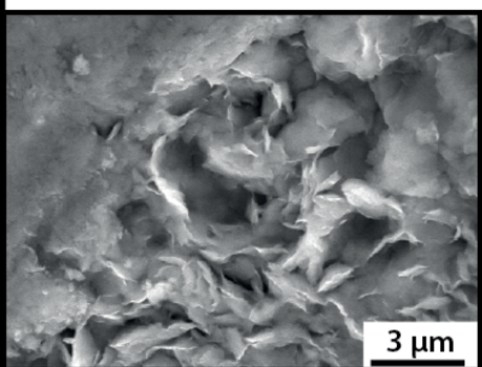
(F) Facies F6 foraminifera bearing muddy facies, moderately rich in foraminifera (*F*) with rare glauconitic grains.

(G) Facies F7 muddy facies, very fine facies poor in foraminifera (*F*).

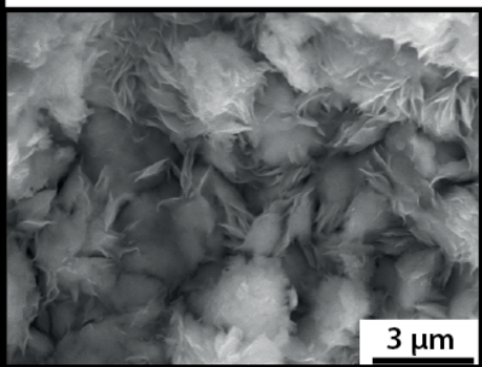




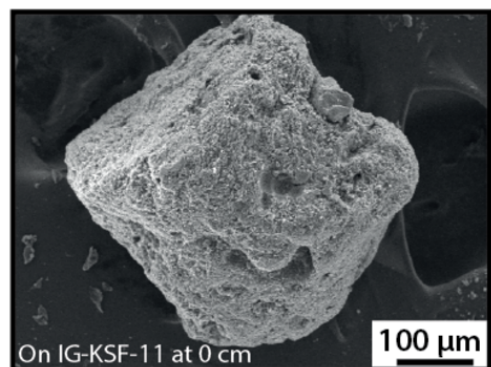
On IG-KSF-11 at 420 cm



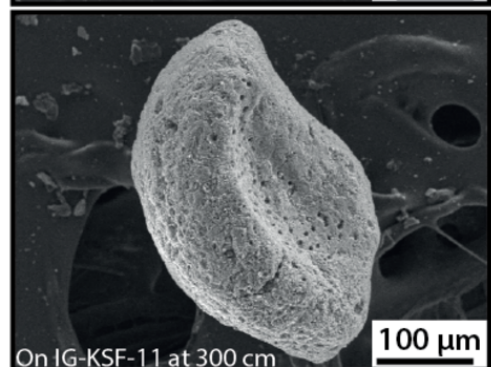
On IG-KSF-11 at 442 cm



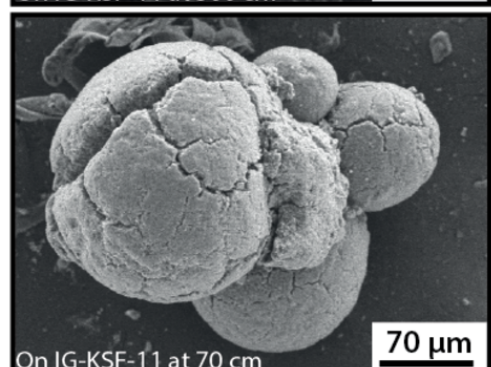
On IG-KSF-11 at 442 cm



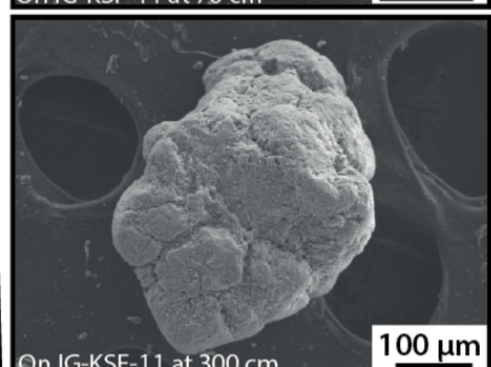
On IG-KSF-11 at 0 cm



On IG-KSF-11 at 300 cm



On IG-KSF-11 at 70 cm



On IG-KSF-11 at 300 cm

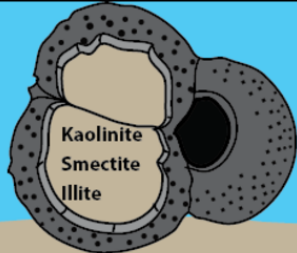
Al_2O_3	9.83 %
MgO	3 %
Fe_2O_3	30.87 %
K_2O	2.99 %

Al_2O_3	6.30 %
MgO	3.50 %
Fe_2O_3	33.43 %
K_2O	3.46 %

Al_2O_3	5.70 %
MgO	4.09 %
Fe_2O_3	33.32 %
K_2O	4.01 %

Al_2O_3	4.05 %
MgO	3.28 %
Fe_2O_3	37.52 %
K_2O	6.54 %

Seawater



Sedimentation and muddy infilling of foraminifera tests

0

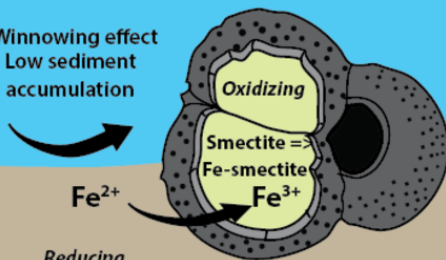
Al_2O_3	18.1 %
MgO	1.6 %
Fe_2O_3	9.0 %
K_2O	2.5 %
Al_2O_3	8.82 %
MgO	2.89 %
Fe_2O_3	26.99 %
K_2O	2.90 %

Sediment

Seawater

1

Winnowing effect
Low sediment accumulation



Fe^{2+}

Reducing

Sediment

Seawater

2

Winnowing effect

Low sediment accumulation

Fe^{2+}

Reducing

Al_2O_3	7.43 %
MgO	3.59 %
Fe_2O_3	30.25 %
K_2O	3.19 %

Sediment

Seawater

3a

Winnowing effect

Low sediment accumulation

Fe^{2+}

K^+

Reducing

Al_2O_3	5.62 %
MgO	3.28 %
Fe_2O_3	33.98 %
K_2O	4.34 %

Sediment

Seawater

3b

Winnowing effect

Low sediment accumulation

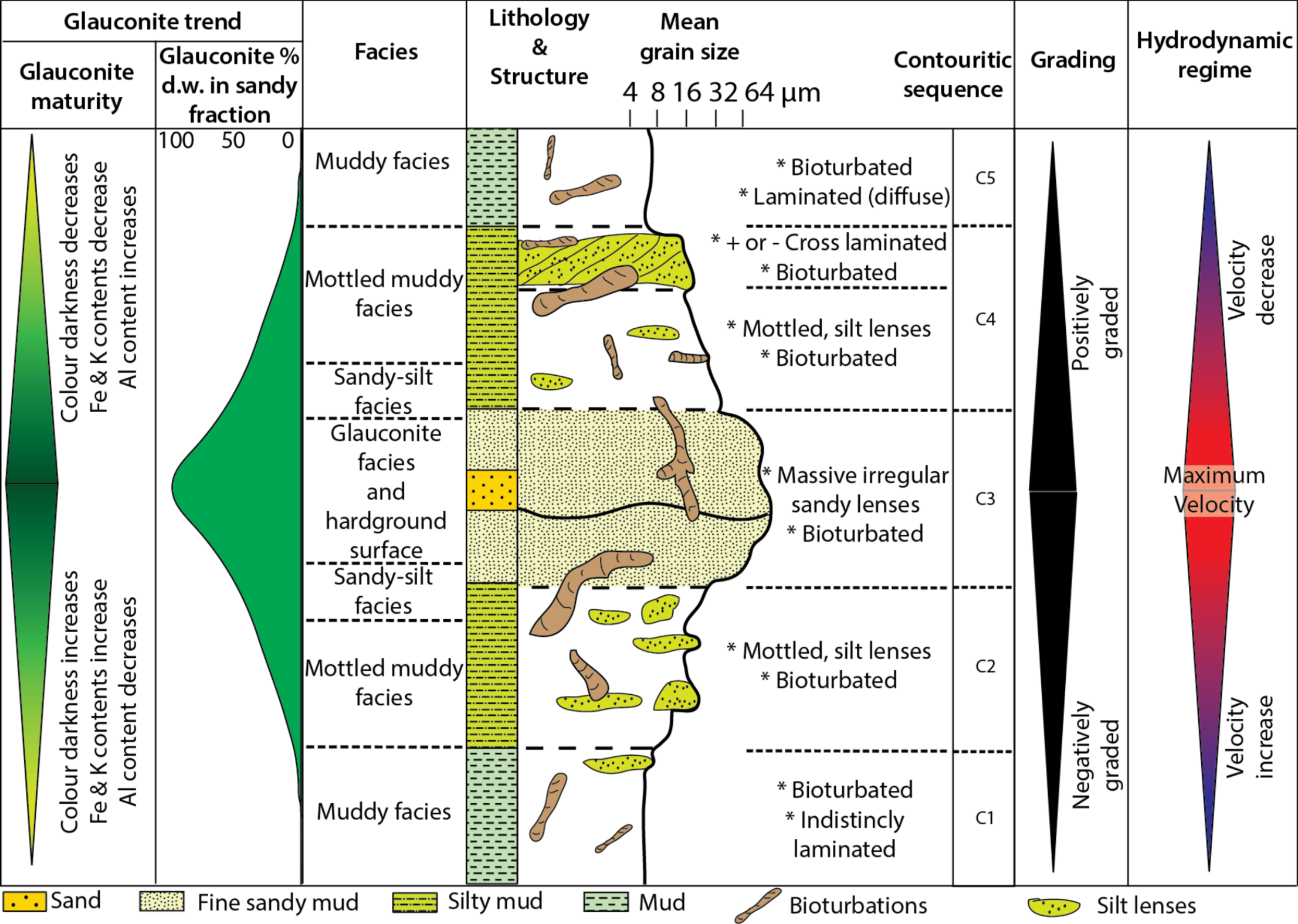
Fe^{2+}

K^+

Reducing

Al_2O_3	5.84 %
MgO	3.13 %
Fe_2O_3	34.18 %
K_2O	5.84 %

Sediment



Depth core (cm)	Core	Material	Age ¹⁴ C (yr BP)	1 sigma calibrated age (yr cal. BP)		
				min	max	average
0	IG-KSF-11	<i>Globigerinoides sp.</i>	13 930 ± 80 BP	14 201	14 466	14 334
60	IG-KSF-11	<i>Globigerinoides sp.</i>	34 400 ± 600 BP	35 630	37 248	36 439
130	IG-KSF-11	<i>Globigerinoides sp.</i>	37 100 ± 800 BP	38 560	39 974	39 267
130	IG-KSF-11	<i>Globigerinoides sp.</i>	50 000 ± 4 000 BP			
313	IG-KSF-11	<i>Globigerinoides sp.</i>	42 700 ± 1 500 BP	42 287	45 138	43 713
452	IG-KSF-11	<i>Globigerinoides sp.</i>	48 000 ± 3 000 BP	-	-	-
530	IG-KSF-11	<i>Globigerinoides sp.</i>	49 000 ± 4 000 BP	-	-	-
530	IG-KSF-11	Mud organic matter	26 170 ± 450 BP	27 519	28 574	28 047
582	IG-KSF-11	<i>Globigerinoides sp.</i>	39 700 ± 1 100 BP	40 675	42 385	41 530
600	IG-KSF-11	<i>Globigerinoides sp.</i>	35 300 ± 700 BP	36 716	38 227	37 472
600	IG-KSF-11	<i>Globigerinoides sp.</i>	28 400 ± 200 BP	29 479	30 059	29 769
0	IG-KSF-05	<i>Globigerinoides sp.</i>	5 640 ± 40 BP	4 027	4 158	4 093
290	IG-KSF-05	<i>Globigerinoides sp.</i>	17 460 ± 100 BP	18 485	18 763	18 624
50	IG-KSF-05	<i>Globigerinoides sp.</i>	34 400 ± 600 BP	34 991	36 551	35 771
169	IG-KSF-05	<i>Globigerinoides sp.</i>	37 910 ± 870 BP	39 262	40 584	39 923
250	IG-KSF-05	<i>Globigerinoides sp.</i>	30 600 ± 400 BP	31 965	32 617	32 291
250	IG-KSF-05	Mud organic matter	24 370 ± 230 BP	26 154	26 661	26 408
340	IG-KSF-05	<i>Globigerinoides sp.</i>	44 000 ± 3000 BP	42 912	47 381	45 147
490	IG-KSF-05	<i>Globigerinoides sp.</i>	41 000 ± 2000 BP	41 339	43 001	42 170
657	IG-KSF-05	<i>Globigerinoides sp.</i>	>43 000 BP	-	-	-

table 1: Radiocarbon dates for well-preserved *Globigerinoides sp.* fractions from samples collected from core IG-KSF-11. The calibrated ages were calculated using Calib 7.0.4 with the Marine 09 calibration curve (Reimer et al., 2013)

IG-KSF-05

Intervals	Duration (kyr)	stade	source
0-18	0-11.7	MIS 1	Martinson et al., 1987; Walter et al., 2009
25-139	11.7-24.1	MIS 2	
139-451	24.1-58.9	MIS 3	
451-590	58.9-74	MIS 4	
?	74-130	MIS 5	

IG-KSF-11

Intervals	Duration (kyr)	stade	source
0-10	0-11.7	MIS 1	Martinson et al., 1987; Walter et al., 2009
10-43	11.7-24.1	MIS 2	
43-80	24.1-58.9	MIS 3	
80-150	58.9-74	MIS 4	
150-267	74-130	MIS 5	
267-371	130-189.6	MIS 6	
371-422	189.6-244	MIS 7	
?			
?	244-291	MIS 8	

Table 2 : Tie points identified in the IG-KSF-05 and IG-KSF-11 core based on correlation with reference oxygen isotope curves (Martinson et al., 1987; Walker et al., 2009)

	Characterisitc	Components	Glaucy maturity	Fracturation of components	Structure	Environment interpretation
F1 - Carbonate facies	Rich in carbonate, indurated mass, low hydratation of sediments	- Rare glaucy -Some iron oxyde - Foramnifera rich		Low to medium	Absence	Mass Transoprt Deposit
F2 - Glaucy facies	Glaucy rich	- Glaucy rich - Foramnifera rich	- Dark green - Clasts	Medium to high	- Bioturbation rich - Sandy foraminifera laminae	Contourites
	Glaucy rich	- Glaucy rich - Foramnifera rich	- Dark green - Inside foramnifera or with foraminifera shape	Medium to high	- Bioturbation rich - Sandy foraminifera laminae	Contourites
F3 - Sandy facies	Foraminifera rich, glaucy in foraminifera	- Glaucy rich - Foramnifera rich - Quartz in bioturbation	- Light to dark green - Inside foramnifera or with foraminifera shape	Medium to high	- Bioturbation rich - Sandy foraminifera laminae	Contourites
F4 - Foraminifera-bearing Muddy facies	Glaucy and foraminifera rich	- Some glaucy - Foramnifera rich -Some iron oxyde - Quartz in bioturbation	- Glaucy in foraminifera test or with foraminifera shape - Light to medium green	Low to medium	Bioturbation rich	Contourites
F5 - Foraminifera sand	Foraminifera rich without glaucy	- Rare foramnifera	- Low glaucy and sometimes none glaucy	Low	Bioturbation rich	Hemipelagite
F6 - Foraminifera bearing Muddy facies	Foraminifera rich with little glaucy	- Rare glaucy - Foramnifera rare -Some iron oxyde	- Low glaucy and sometimes none glaucy	Low	- Bioturbation rich - Sandy foraminifera lenses	Hemipelagite
F7 - Muddy facies	Very fine matrix and grains poor	- Rare glaucy - Foramnifera rare -Some iron oxyde	- Low glaucy and sometimes none glaucy	Low	Low to high Bioturbation	Hemipelagite

	Al₂O₃	MgO	Fe₂O₃	K₂O	SiO₂
Mud	18.1%	1.6%	9.0%	2.5%	46.8%
Greenish/ yellowish grain	8.8%	2.9%	27.0%	2.9%	47.1%
Green grain	7.4%	3.6%	30.3%	3.2%	51.2%
Dark green grain	5.6%	3.3%	34.0%	4.3%	49.1%
Very dark green grain	5.8%	3.1%	34.2%	5.4%	48.6%

Table 4 : Average chemical composition measured by microprobe coupled to the SEM on mud and on green grains coming from the core IG-KSF-11 at different depth on the core (0 cm, 60 cm, 70 cm, 90 cm, 300 cm, 420 cm, 442 cm, 460 cm, 590 cm).